JOURNAL OF GEOPHYSICAL RESEARCH, VOL. 112, B06304, doi:10.1029/2006JB004505, 2007

Compressible thermochemical convection and application to lower mantle structures

Eh Tan[1,2] and Michael Gurnis[1]

Received 13 May 2006; revised 2 December 2006; accepted 14 February 2007; published 13 June 2007.

[1] A new finite element code for compressible thermochemical convection is developed to study the stability of a chemical layer at the base of the mantle. Using composition-dependent compressibility and a density difference between compositions at a reference pressure, a composition-dependent density profile is derived. Together with depth-dependent thermal expansion, this combination of parameters yields a wide range of dynamic evolutions for the chemical layer. The chemical structures are classified into five major categories (classical plumes, mushroom-shaped plume, domes, ridges, and continuous layers) and a few abnormal cases, such as hourglass-shaped plumes and columnar plumes. Several models have a chemical structure morphologically similar to the African low V_S structure in the lower mantle, at least at a single time. Guided by our models, several dynamic scenarios are proposed for the dynamic nature of the lower mantle low-velocity structures (a.k.a. superplumes), including plumes at an early stage, plume clusters, ridges, passive piles, sluggish domes, and high-bulk-modulus domes. We predict seismic velocity anomalies from these dynamic models. The thermoelastic parameters used in the conversion are additional constraints. We compare the density structure with normal mode inversion, the predicted seismic signature observations, and the required thermoelastic parameters with mineral physics data. Among the proposed scenarios, only the scenario of high-bulk-modulus domes satisfies all constraints simultaneously. The implication on the geochemistry and mineralogy of lower mantle chemical structures is discussed.

Citation: Tan, E., and M. Gurnis (2007), Compressible thermochemical convection and application to lower mantle structures, *J. Geophys. Res.*, *112*, B06304, doi:10.1029/2006JB004505.

1. Introduction

[2] The large density contrast between the mantle and core, the largest in Earth's interior, facilitates the accumulation of chemical heterogeneity. Seismic images show strong seismic velocity variations at the base of the mantle (cf. reviews by *Lay et al.* [1998] and *Garnero* [2000]). The seismic velocity variation is too strong to be explained solely by temperature variation [*Karato and Karki*, 2001] and must involve phase or compositional variations, or some combination.

[3] There are three possible phase changes in the lower mantle. Two of them have been associated with seismic observations. The D″ discontinuity [*Lay and Helmberger*, 1983], attributed to the perovskite to postperovskite phase change [*Sidorin et al.*, 1999b; *Murakami et al.*, 2004; *Oganov and Ono*, 2004], and the ultralow-velocity zones (ULVZs) [*Garnero and Helmberger*, 1996], attributed to partial melting [*Williams and Garnero*, 1996; *Wen and Helmberger*, 1998; *Rost et al.*, 2005], are evidences of phase heterogeneity. The third phase change, the high to low spin transition of Fe [*Badro et al.*, 2004], is another potential source of phase heterogeneity. The transition of this phase change may span a broad range of pressures [*Sturhahn et al.*, 2005]. If so, this phase change will not constitute a sharp seismic discontinuity and could be difficult to observe seismologically.

[4] Chemical heterogeneity in the lower mantle has been proposed as an explanation for observed isotopic heterogeneity in oceanic basalts [*Allegre et al.*, 1980]. To satisfy isotopic observations, chemical reservoirs must be isolated from the upper mantle for billions of years [*Brooks et al.*, 1976]. Earlier, much of this chemical heterogeneity was thought to be associated with the seismic discontinuity at 660-km depth [*Jacobsen and Wasserburg*, 1979]. Advances in seismic tomography, showing images of subducted slabs penetrating into the lower mantle, excludes chemical layering at 660-km depth [*Grand et al.*, 1997; *van der Hilst et al.*, 1997]. A deeper chemical boundary at 1000- to 1500-km depth with high relief was later proposed [*Kellogg et al.*, 1999]. Such a chemical boundary, accompanied with a hot thermal boundary layer, should be observable by seismic tomography [*Tackley*, 2002], but none has been found at this depth [*Castle and van der Hilst*, 2003].

[1] Seismological Laboratory, California Institute of Technology, Pasadena, California, USA.
[2] Now at Computational Infrastructure for Geodynamics, Pasadena, California, USA.

0148-0227/07/2006JB004505$09.00

[5] Tomography reveals a degree-2 pattern of seismic velocity anomalies near the bottom of the mantle [*Grand et al.*, 1997; *Su and Dziewonski*, 1997; *van der Hilst et al.*, 1997; *Ritsema et al.*, 1999; *Kuo et al.*, 2000; *Masters et al.*, 2000; *Megnin and Romanowicz*, 2000; *Montelli et al.*, 2004; *Trampert et al.*, 2004]. Two prominent regions with low seismic velocity are found beneath southern Africa and the southwestern Pacific, surrounded by high seismic velocities. The high-velocity anomalies, whose geographic location matches ancient subduction zones, have been interpreted as subducted slabs [*Richards and Engebretson*, 1992] and thought to be colder than the regions they surround. On the other hand, both low-velocity regions display large positive geoid anomalies, shallow seafloor and elevated topography, and extensive hot spot volcanism [*Nyblade and Robinson*, 1994; *McNutt*, 1998]. Together with a correlation with the erupted location of Large Igneous Provinces [*Burke and Torsvik*, 2004], these observations suggest that the low-velocity seismic structures are warmer than surrounding mantle. These regions have been called "superplumes," implying that they are buoyant upwellings. However, the dynamic nature of these regions remains uncertain and is the main theme of this study. We refer to these regions as low-velocity structures (LVSs).

[6] The anticorrelation of shear wave velocity anomaly δV_S with bulk sound velocity anomaly δV_ϕ [*Su and Dziewonski*, 1997; *Ishii and Tromp*, 1999; *Masters et al.*, 2000], anti-correlation of δV_S and density anomaly $\delta\rho$ [*Ishii and Tromp*, 1999, 2004; *Resovsky and Trampert*, 2003], spatially sharp reductions in shear wave velocity V_S [*Wen*, 2001; *Ni et al.*, 2002; *To et al.*, 2005], and spatial correlation with geochemical anomalies [*Castillo*, 1988] suggest that the LVSs have a composition distinct from ambient mantle. The sharp reduction in V_S indicates the presence of a chemical boundary. Moreover, the chemical boundary of the southern African LVS is found to extend at least 1000 km above the core-mantle boundary (CMB) with a width of 1000 km and a length of 7000 km [*Ni et al.*, 2002; *Ni and Helmberger*, 2003a, 2003b, 2003c], although the exact shape and height are not yet well constrained. The average δV_S of the southern African LVS is about -3%, while the average compressional wave velocity anomaly δV_P is about -0.5%. The morphological and seismic signatures of this part of the African LVS are diagnostic of its dynamics. Another potentially important diagnostic is that LVSs are denser than its surroundings [*Ishii and Tromp*, 1999, 2004; *Resovsky and Trampert*, 2003], although the veracity of this inference is debated [*Romanowicz*, 2001; *Kuo and Romanowicz*, 2002]. The African LVS is sometimes described as a "ridge" based on its elongated horizontal extent [e.g., *Ni and Helmberger*, 2003b; *McNamara and Zhong*, 2005]. However, in this paper, we reserve the word "ridge" to a structure with a triangular vertical cross section.

[7] The fate of a dense chemical layer at the base of the convecting mantle has been investigated extensively [*Christensen*, 1984; *Gurnis*, 1986; *Hansen and Yuen*, 1988; *Olson and Kincaid*, 1991; *Farnetani*, 1997; *Tackley*, 1998; *Davaille*, 1999; *Montague and Kellogg*, 2000; *Gonnermann et al.*, 2002; *Jellinek and Manga*, 2002; *Ni et al.*, 2002; *Namiki*, 2003; *McNamara and Zhong*, 2004, 2005]. A chemical layer, stabilized by an intrinsic density anomaly $\Delta\rho_{ch}$, tends to remain at the CMB. Later, as the layer heats up, its density decreases by $\Delta\rho_{th}$. The (negative) thermal density anomaly $\Delta\rho_{th}$, which is proportional to $\rho_r\alpha\delta T$, depends on the reference density ρ_r, the coefficient of thermal expansion α, and the temperature anomaly of the material δT. The net density anomaly is $\Delta\rho_{ch} - \Delta\rho_{th}$. The chemical and thermal effects compete in controlling the stability of the layer. Consider a parcel of chemically anomalous material at the CMB: As the parcel heats up, δT increases, and so does $\Delta\rho_{th}$. When $\Delta\rho_{th}$ becomes equal to or greater than $\Delta\rho_{ch}$, the parcel becomes unstable and rises upward. The parcel can lose heat by thermal diffusion or adiabatic cooling during ascent and subsequently restabilize. The change in stability depends on the rate of heat loss and the depth dependence of various aforementioned parameters.

[8] Composition-dependent rheology has been shown to stabilize the chemical layer [*Davaille*, 1999; *McNamara and Zhong*, 2004]. When the chemical layer has a higher intrinsic viscosity than ambient, the layer forms domes, which can rise and then sink cyclically several times. This dynamic scenario has been invoked to explain the African LVS [*Davaille et al.*, 2005].

[9] When $\Delta\rho_{ch}$ is small, the layer becomes unstable with a small temperature increase, eventually forming a thermochemical plume, such that the layer becomes stirred with the rest of the mantle. On the other hand, when $\Delta\rho_{ch}$ is sufficiently large, the layer remains stable with small topography on the interface between the intrinsically dense and ambient regions. Only when $\Delta\rho_{ch}$ is within a narrow range of intermediate values can the layer have high topography on its interface.

[10] In most previous studies, the reference density and coefficient of thermal expansion were assumed to be constant with depth. However, the compression at the large pressure of the lower mantle increases the density and decreases the coefficient of thermal expansion. From the Preliminary Reference Earth Model (PREM) [*Dziewonski and Anderson*, 1981], the average density increases from 3380 kg/m^3 at the base of lithosphere to 5560 kg/m^3 at the CMB. The coefficient of thermal expansion of the mantle is 5×10^{-5} K^{-1} at the base of lithosphere. The magnitude of the coefficient of thermal expansion in the lower mantle is not as well known. At 2000-km depth, for example, the coefficient of thermal expansion for perovskite is estimated to be 1.5×10^{-5} K^{-1} [*Oganov et al.*, 2001] or 1.3×10^{-5} K^{-1} [*Marton and Cohen*, 2002]. The coefficients of thermal expansion of several types of mantle rock have been estimated to have a similar value of 1.3×10^{-5} K^{-1} [*Hama and Suito*, 2001]. Consequently, the product of $\rho_r\alpha$ decreases with depth, and the stability of chemically anomalous material will be depth-dependent.

[11] In most previous studies, the chemical density anomaly is assumed to be constant with depth. However, materials with different compressibility will have different adiabatic density profiles. Highly compressible (low bulk modulus) material has a steeper adiabatic density profile than less compressible (high bulk modulus) material. The difference between the density profiles is the chemical density anomaly profile. As a result, after accounting for compressibility, the chemical density profile can be depth-dependent.

[12] Considering a mantle with an anomalous chemical composition, which has a depth-dependent thermal density anomaly and is warmer than its surroundings, the lower portion of the structure is denser than the surrounding

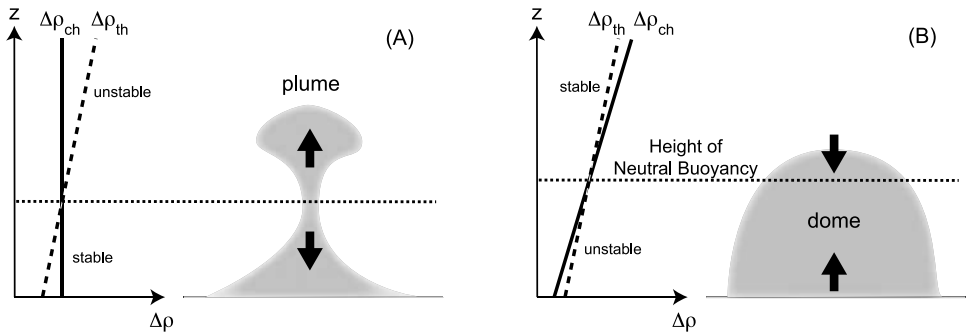

Figure 1. Density anomaly profiles. (A) When $\Delta\rho_{ch}$ is constant with depth, at some depth, the chemical and thermal density anomalies are equal and the net density anomaly is 0. The net density anomaly is negative above the depth and positive below. (B) When $\Delta\rho_{ch}$ is also depth-dependent, and changes faster than $\Delta\rho_{th}$, the trend of the density profile can be reversed. The net density anomaly is positive above the HNB and negative below.

mantle while the upper portion is less dense (Figure 1a). At some depth, the chemical and thermal density anomalies are equal and the net density anomaly is 0. The net density anomaly is negative above that depth but positive below. Material above this depth tends to move upward and becomes even less stable as it does so. Material below this depth tends to move downward, becoming more stable. As a result, the upper portion of the chemical structure will become a plume, while the lower portion will become a flat layer with a cusp. The conclusion of this simple analysis suggests that a stable thermochemical structure with high topography is difficult to produce with an Earth-like thermal expansion profile [*Ni et al.*, 2002].

[13] On the other hand, if $\Delta\rho_{ch}$ is not constant and changes faster than $\Delta\rho_{th}$, the trend of density profile can reverse. The height above the CMB where the chemical and thermal density anomalies are equal is called the height of neutral buoyancy (HNB). The net density anomaly is positive above the HNB but negative below. The lower portion of the chemical structure is less dense and rises. Both the thermal and chemical density anomalies increase during the ascent. If the later increases faster than the former, upon rising above the HNB, the chemically anomalous material becomes denser than the surrounding mantle and starts sinking (Figure 1b). With this scenario, a heated dense material can form a dome with high relief [*Tan and Gurnis*, 2005].

[14] Although the mantle is compressible, most dynamic models utilize the Boussinesq approximation (an approximation for incompressible flow) for mathematical and numerical simplicity. Various compressible convection models have been developed [*Jarvis and McKenzie*, 1980; *Baumgardner*, 1985; *Glatzmaier*, 1988; *Machetel and Yuen*, 1989; *Schmeling*, 1989; *Steinbach et al.*, 1989; *Leitch et al.*, 1991; *Quareni et al.*, 1991; *Balachandar et al.*, 1992; *Bercovici et al.*, 1992; *Ita and King*, 1994; *Solheim and Peltier*, 1994; *Tackley*, 1996; *Zhang and Yuen*, 1996; *Bunge et al.*, 1997]. The main effect of compressibility is to introduce adiabatic density and temperature gradients, which reduce the vigor of convection. However, when variation in chemical composition is included, another effect of compressibility can significantly change the pattern of the convection. The density contrast between materials of different compressibility and therefore of different density profiles can vary in magnitude and sign as a function of depth. As a result, compressible thermochemical convection models exhibit complex dynamics not seen in incompressible thermochemical convection models [*Xie and Tackley*, 2004; *Nakagawa and Tackley*, 2005; *Farnetani and Samuel*, 2005; *Tan and Gurnis*, 2005].

[15] In this paper, we will describe our numerical methods for compressible thermochemical convection. We will systematically explore the effect of composition-dependent density profiles and depth-dependent thermal expansion on the stability of a basal dense chemical layer. We find a wide range of dynamic evolution for the chemical layer. Several models have a chemical structure morphologically similar to the LVSs. We convert these dynamic models into seismic velocity anomalies. The thermoelastic parameters used in the conversion are additional useful constraints. We compare the seismic signature of the converted model with seismic observation and the required thermoelastic parameters with mineral physics data to find the preferred dynamic models.

2. Methods

[16] We use the truncated anelastic liquid approximation (TALA [*Ita and King*, 1994]) as the governing equations in two-dimensional (x, z) Cartesian coordinate system. All equations are nondimensional. The continuity equation is

$$\nabla \cdot (\rho_r \mathbf{u}) = 0 \tag{1}$$

where $\mathbf{u} = (u_x, u_z)$ is the velocity vector and $\rho_r = \rho_r(z)$ is the reference density profile.

[17] The momentum equation is

$$-\nabla P + \nabla \cdot \underline{\tau} = \varepsilon_T^{-1}(\Delta\rho_{ch} C - \varepsilon_T \rho_r \alpha T) g Ra \mathbf{e}_z \tag{2}$$

where P is the dynamic pressure, τ is the deviatoric stress tensor, ε_T is a nondimensional number related to thermal expansion (defined later), $\Delta\rho_{ch} = \Delta\rho_{ch}(z)$ is the chemical density anomaly profile, C is the concentration (between 0 and 1) of the anomalous material, $\alpha = \alpha(z)$ is the coefficient of thermal expansion, T is the temperature, g is the gravity, Ra is the Rayleigh number, and $\mathbf{e}_z$ is the unit vector in the vertical direction pointing upward. The term inside the paren-

theses is the net density anomaly $\Delta\rho$. In TALA, the effect of the dynamic pressure on the density is ignored, as justified previously [*Jarvis and McKenzie*, 1980]. The Rayleigh number is defined as $Ra = \rho_0 g_0 \alpha_0 \Delta T_{\text{total}} h^3/\kappa_0\eta_0$, where ρ_0 is the characteristic density, g_0 is the characteristic gravity, α_0 is the characteristic coefficient of thermal expansion, ΔT_{total} is the total temperature contrast, h is the depth of the computational domain, κ_0 is the characteristic thermal diffusivity, and η_0 is the characteristic viscosity.

[18] The energy equation is

$$\rho_r C_P \frac{\partial T}{\partial t} = -\rho_r C_P \mathbf{u}\cdot\nabla T + \nabla\cdot(k_T \nabla T) + Di(T+T_s)\rho_r \alpha g u_z + \frac{Di}{Ra}\underline{\tau}:\underline{\varepsilon} + \rho_r H \tag{3}$$

where C_P is the heat capacity at constant pressure, t is the time, k_T is the thermal conductivity, Di is the dissipation number, T_s is the surface temperature, ε is the deviatoric strain rate tensor, and H is the internal heating rate. The right-hand side terms are the advection, diffusion, adiabatic cooling, viscous dissipation, and internal heating, respectively. The dissipation number is defined as $Di = \alpha_0 g_0 h/C_{P0}$, where C_{P0} is the characteristic heat capacity at constant pressure.

[19] The constitutive relationship is

$$\underline{\tau} = 2\eta\left(\underline{\varepsilon} - \frac{1}{3}(\nabla\cdot\mathbf{u})\underline{I}\right) \tag{4}$$

where η is the viscosity and $\underline{I}$ is the identity tensor. The components of the deviatoric strain rate tensor are

$$\varepsilon_{xx} = \frac{\partial u_x}{\partial x}, \quad \varepsilon_{zz} = \frac{\partial u_z}{\partial z}, \quad \varepsilon_{xz} = \varepsilon_{zx} = \frac{1}{2}\left(\frac{\partial u_x}{\partial z} + \frac{\partial u_z}{\partial x}\right) \tag{5}$$

Two other useful nondimensional parameters are the Gruneisen parameter $\gamma = \alpha_0 K_{S0}/\rho_0 C_{P0}$, where K_{S0} is the characteristic bulk modulus, and the fraction of volume change due to thermal expansion $\varepsilon_T = \alpha_0 \Delta T_{\text{total}}$.

[20] We modified the finite element code ConMan [*King et al.*, 1990] by incorporating compressibility. The original code uses the penalty function formulation [*Hughes*, 2000], where pressure is treated as a dependent variable of velocity, and the stiffness matrix is penalized by the pressure term. Our modified code uses the mixed method formulation [*Hughes*, 2000], where velocity and pressure are treated as independent variables. The stiffness matrix is assembled from each element stiffness matrix k^e. k^e can be written as

$$k^e = \mathop{\mathbf{A}}_{a,b\ i,j}\left[e_i^T\left(\int_{\text{element}} B_a^T D_\eta B_b \mathrm{d}\right)e_j\right] \tag{6}$$

where $\mathbf{A}$ is the assembling operator, indices a and b are the elemental node indices, indices i and j are the directional indices, and e_i and e_j are the unit direction vectors. B_a and D_η are defined as

$$B_a = \begin{bmatrix} N_{a,x} & 0 \\ 0 & N_{a,y} \\ N_{a,z} & N_{a,x} \end{bmatrix} \tag{7}$$

$$D_\eta = \eta\begin{bmatrix} 4/3 & -2/3 & 0 \\ -2/3 & 4/3 & 0 \\ 0 & 0 & 1 \end{bmatrix} \tag{8}$$

where N_a and N_b are the shape functions of nodes a and b, respectively; $N_{a,x}$ and $N_{a,y}$ are the partial derivatives of N_a in the x and y direction, respectively. Note that the element stiffness matrix is different from the formulation of *King et al.* [1990] in two ways. The element stiffness matrix is not penalized by the pressure term and contains the contribution of volumetric change due to compression.

[21] Equation (1) can be rearranged as

$$\nabla\cdot\mathbf{u} + \frac{1}{\rho_r}\frac{\partial\rho_r}{\partial z}u_z = 0 \tag{9}$$

After discretization, the resultant matrix equations of equations (2) and (9) become

$$\begin{bmatrix} K & B^T \\ B + C_\beta & 0 \end{bmatrix}\begin{bmatrix} u \\ p \end{bmatrix} = \begin{bmatrix} b \\ 0 \end{bmatrix} \tag{10}$$

where K is the stiffness matrix, B is the divergence operator, whose transpose B^T is the gradient operator, C_β is a constant matrix corresponding to the second term in equation (9), and b is the force vector. This matrix system is asymmetric because of the nonzero C_β. We adapted the pressure correction algorithm [*Ramage and Wathen*, 1994] and used the biconjugate gradient stabilized method [*Barrett et al.*, 1994] to solve the equations iteratively. The algorithm is described in Table 1. The inverse of the stiffness matrix K^{-1} is calculated outside the iteration loop. As a result, computing each iteration involves only matrix-vector and vector-vector contractions. We developed an analytical solution for compressible convection and benchmarked our numerical result with the analytical result (Appendix A).

[22] The energy equation (3) is solved using a streamline upwind Petrov-Galerkin scheme [*Brooks and Hughes*, 1982]. Each term on the right-hand side of equation (3), except the viscous dissipation, is computed on the element level. The viscous dissipation is calculated using nodal stress and strain rate to improve numerical accuracy. The solution of the energy equation is benchmarked in Appendix B.

[23] The composition field is computed using the marker chain method [*Davies and Gurnis*, 1986; *van Keken et al.*, 1997]. The marker chain is advected using a fourth-order predictor-corrector scheme. If the distance between two adjacent markers is greater than a predefined threshold, a new marker is inserted in between them. The marker chain

Table 1. Algorithm to Solve Equation (10)[a]

$p_0 = 0$	Initialize pressure vector
$u_0 = K^{-1}\, b$	Initial guess of velocity
$r_0 = (B + C_\rho)\, u_0$	Calculate initial residual
$z = r_0$	Choose conjugate residual
$i = 1$	Initialize iteration count
$\rho_0 = 1$	
Begin loop	Start iteration
$\rho_i = (z, r_{i-1})$	Compute convergence criterion
If $\rho_i = 0$, method fails	
If $\rho_i < \varepsilon$, stop loop	ε is a small positive number
If $i = 1$	
$q_i = r_{i-1}$	Initial search direction for pressure
Else	
$\beta = (\rho_i/\rho_{i-1})(\alpha_{i-1}/\omega_{i-1})$	
$q_i = r_{i-1} + \beta\,(q_{i-1} - \omega_{i-1} d_{i-1})$	Update pressure search direction
End if	
$v_i = K^{-1} B^{\mathrm{T}} q_i$	New search direction for velocity
$d_i = (B + C_\rho) v_i$	New search direction for pressure
$\alpha_i = \rho_i/(z, d_i)$	Set step length
$s = r_{i-1} - \alpha_i d_i$	Update residual
If norm(s) is too small, stop loop	If the norm of s is too small, further update will not be beneficial
$w_i = K^{-1} B^{\mathrm{T}} s$	New search direction for velocity
$t = (B + C_\rho) w_i$	New search direction for pressure
$\omega_i = (t, s)/(t, t)$	Set step length
$p_i = p_{i-1} + \alpha_i q_i + \omega_i s$	Update pressure
$u_i = u_{i-1} - \alpha_i v_i - \omega_i w_i$	Update velocity
$r_i = s - \omega_i t$	Update residual
$i = i + 1$	Update iteration count
End loop	

[a]Symbols used here are not related to symbols in other equations.

defines the material interface. Because of material entrainment, the length of the marker chain grows exponentially with time. The computational efficiency of the marker chain method severely deteriorates if there is substantial material entrainment, in which case we halt the computation. For some halted models, the marker chain is trimmed to remove excess entrainment, and the computation restarted in order to proceed further. The trimming of the marker chain introduces error in the composition field, but the magnitude of the error is estimated to be small and does not influence the stability of the chemical layer.

[24] Potentially, thermodynamics and transport properties of chemically distinct materials could be composition-dependent. For the sake of simplicity, only the bulk modulus and density are assumed compositionally dependent. The adiabatic density of the ambient mantle (material 1) ρ_{S1} is calculated by integrating the self-compression equation

$$\begin{aligned} \mathrm{d}P_{\mathrm{H}} &= -\rho_{\mathrm{r}} g \mathrm{d}z \\ \mathrm{d}\rho_{S1} &= \frac{Di}{\gamma}\frac{\rho_{S1}}{K_{S1}}\mathrm{d}P_{\mathrm{H}} \\ \rho_{S1} &= 1, \text{ at } z = 1 \end{aligned} \tag{11}$$

where $P_{\mathrm{H}} = P_{\mathrm{H}}(z)$ is the hydrostatic pressure, and $K_{S1} = 1$ is the bulk modulus of the ambient mantle. The reference density profile ρ_{r} is set as ρ_{S1}. The adiabatic density ρ_{S2} of the anomalous material (material 2) with bulk modulus K_{S2} is calculated by

$$\begin{aligned} \mathrm{d}\rho_{S2} &= \frac{Di}{\gamma}\frac{\rho_{S2}}{K_{S2}}\mathrm{d}P_{\mathrm{H}} \\ \rho_{S2} &= 1 + \rho_{\mathrm{top}}, \text{ at } z = 1 \end{aligned} \tag{12}$$

The density differences at the top surface $\Delta\rho_{\mathrm{top}}$ and K_{S2} vary between models. The chemical density profile $\Delta\rho_{\mathrm{ch}} = \rho_{S2} - \rho_{S1}$ is the difference between ρ_{S2} and ρ_{S1}. The nondimensional parameter $\Delta\rho_{\mathrm{top}}/\rho_0\varepsilon_{\mathrm{T}}$ is commonly referred to as the buoyancy number.

[25] Different combinations of ρ_{top} and K_{S2} can produce chemical density profiles of different slopes $\mathrm{d}\Delta\rho_{\mathrm{ch}}/\mathrm{d}z$. For example, fixing K_{S2} while increasing $\Delta\rho_{\mathrm{top}}$ will change the slope of $\Delta\rho_{\mathrm{ch}}$ from positive to zero and finally to negative (Figure 2a). On the other hand, fixing $\Delta\rho_{\mathrm{top}}$ while increasing K_{S2} will change the slope from negative to zero and finally to positive (Figure 2b). We do not consider cases of $K_{S2} < 1$ because seismic observations require the LVSs to have high K_{S} (see section 4.3).

[26] The coefficient of thermal expansion varies linearly in z in the models, $\alpha = \alpha_{\mathrm{CMB}} + m_\alpha z$, instead an anharmonic equation [*Anderson*, 1967], for simplicity. The coefficient of thermal expansion at the CMB, α_{CMB}, is fixed in all models, corresponding to $0.9 \times 10^{-5}\ \mathrm{K}^{-1}$ [*Davies*, 1999, Table 7.3]. We fix the value of α_{CMB} because of the direct trade-off with $\Delta\rho_{\mathrm{top}}$. Increasing both α_{CMB} and $\Delta\rho_{\mathrm{top}}$ will increase $\Delta\rho_{\mathrm{th}}$ and $\Delta\rho_{\mathrm{ch}}$, respectively. Since the stability is affected by the difference between $\Delta\rho_{\mathrm{th}}$ and $\Delta\rho_{\mathrm{ch}}$, changing both density anomalies in the same direction will not affect the dynamics substantially. Therefore we vary $\Delta\rho_{\mathrm{top}}$ while

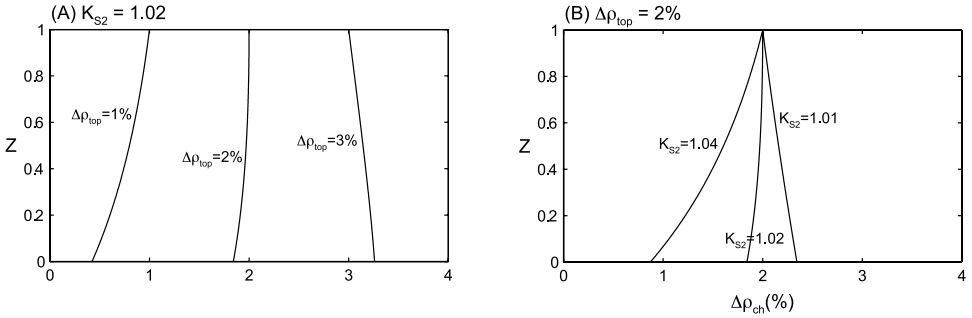

Figure 2. Various chemical density profiles. (A) $K_{S2} = 1.02$, $\Delta\rho_{\mathrm{top}} = 1$–$3\%$. The slope of $\Delta\rho_{\mathrm{ch}}$ changes from positive to vertical and finally to negative. (B) $\Delta\rho_{\mathrm{top}} = 2\%$ $K_{S2} = 1.01$–1.04. The slope of $\Delta\rho_{\mathrm{ch}}$ changes from negative to vertical and finally to positive.

fixing α_{CMB}. The value of m_α varies between models. We did not incorporate composition-dependent thermal expansion in the models because α of lower mantle materials remain poorly constrained.

[27] The viscosity is temperature- and depth-dependent according to the equation

$$\eta = \exp\left(\frac{E_\eta + V_\eta(1-z)}{T+T_\eta} - \frac{E_\eta}{T_\eta}\right) \quad (13)$$

where E_η is the activation energy, V_η is the activation volume, and T_η is the temperature offset. The magnitude of this depth dependence is chosen to compensate for the effect of adiabatic temperature gradients. The viscosity has a minimum cutoff of 10^{-3}.

[28] In this study, we only consider variation in the adiabatic density profile ρ_r and the coefficient of thermal expansion α. Other physical properties are assumed constant with depth and composition. The difference between the thermal and chemical buoyancies drives the convection. Variations in the depth and composition dependence of ρ_r and α change the chemical and thermal buoyancies, respectively. These parameters potentially can reverse the sign of the buoyancy and greatly change the flow pattern. Other material properties (for example, thermal diffusivity, heat capacity, and viscosity) are not directly involved in the buoyancy term. Although these material properties can be depth- and composition-dependent, they can affect the flow through changing the local Rayleigh number. The magnitude of the buoyancy might change, but not the sign. Therefore the profiles of ρ_r and α have a profound influence on the flow pattern.

[29] We have not incorporated any phase change into our calculation. The existence of partial meltings, inferred from ULVZs, is confined at the very base of the mantle, maybe ~40 km above the CMB, and is localized horizontally. The dynamic consequence of ULVZs on lower mantle convection is probably insignificant, except for the plume conduits [*Jellinek and Manga*, 2002]. Another phase change, the postperovskite (PPV) phase change, has a positive Clapeyron slope (8–10 MPa/K) and a 120-GPa transition pressure (corresponding to 200 km above the CMB) [*Tsuchiya et al.*, 2005]. Inside the chemical layer, the temperature could be so high that the PPV phase transition pressure is higher than that at the CMB. Actually, the D″ discontinuity, thought to be caused by the PPV phase change, is rarely observed in the LVSs [*Helmberger et al.*, 2005]. The compositional dependence of the PPV phase change is actively being studied [*Mao et al.*, 2004; *Akber-Knutson et al.*, 2005; *Caracas and Cohen*, 2005; *Murakami et al.*, 2005; *Ono and Oganov*, 2005; *Hirose et al.*, 2006]. This phase change will destabilize the basal thermal boundary layer [*Sidorin et al.*, 1999a; *Nakagawa and Tackley*, 2004].

[30] The computational domain is a 2 × 1 box with its bottom corresponding to the CMB. In some cases, a 6 × 1 box is used. When scaled, the top of the box is 2000 km above the CMB. The size of the box allows us to concentrate on lower mantle dynamics without the complexity of transition zone phase changes or subducted slabs. The top and bottom boundaries are free-slip and isothermal, with fixed temperature at 0 and 1, respectively. The sidewalls are reflecting. The initial temperature is adiabatic with a thin, basal thermal boundary layer. The chemical layer is initially flat with a thickness d. The values of all parameters are listed in Table 2.

Table 2. Values of Parameters in Models

Symbol	Description	Value
ρ_0	Characteristic density	4000 kg/m^3
g_0	Characteristic gravity	10 m/s^2
α_0	Characteristic coefficient of thermal expansion	3×10^{-5} K^{-1}
ΔT_{total}	Total temperature contrast	1800 K
h	Depth of computation domain	2000 km
κ_0	Characteristic thermal diffusivity	1.27×10^{-6} m^2/s
η_0	Characteristic viscosity	10^{22} Pa s
C_{P0}	Characteristic heat capacity at constant pressure	1500 kJ/kg
K_{S0}	Characteristic bulk modulus	266.6 GPa
H	Internal heating	0
Ra	Rayleigh number	2.2×10^6
Di	Dissipation number	0.4
γ	Gruneisen parameter	1.333
T_s	Surface temperature	0.75
ε_T	Fraction of volume change due to thermal expansion	0.054
α_{CMB}	Coefficient of thermal expansion at the CMB	0.3
E_η	Activation energy of viscosity	11
V_η	Activation volume of viscosity	−1.8
T_η	Temperature offset of viscosity	−1.5
d	Initial thickness of chemical layer	0.125

3. Results

[31] We systematically explore the effect of K_{S2}, $\Delta\rho_{top}$, and m_α on the stability of the dense chemical layer. To gauge the parameter space, we estimate the height of neutral buoyancy (HNB) from a simple heuristic calculation. We calculate $\Delta\rho_{ch}$ using equations (11) and (12) and $\Delta\rho_{th} = \varepsilon_T\rho_{S2}\alpha\delta T$ by assuming $\delta T = 0.7$. In dynamic models, δT varies with depth and between models, so the estimated HNB may not coincide with the real HNB. Nevertheless, this calculation represents a useful gauge of the parameter space. The two density anomaly profiles are compared. The HNB is defined as the height from the CMB where $\Delta\rho_{ch}$ and $\Delta\rho_{th}$ are equal. Another requirement of the HNB is that $\Delta\rho_{ch}$ must be less than $\Delta\rho_{th}$ below the height. We do not refer to this height as HNB when $\Delta\rho_{ch}$ is greater than $\Delta\rho_{th}$ below the crossover. For example, there is no HNB in Figure 1a. We compute the estimated HNB in the three-dimensional parameter space (Figure 3a). Later, we will see that the dynamic evolution of the chemical layer is primarily determined by the HNB and the value of $\Delta\rho_{ch}$ at the CMB, $\Delta\rho_{CMB}$.

[32] It is clear from Figure 3a how the estimated HNB is affected by the three parameters. The estimated HNB is sensitive to the value of $\Delta\rho_{top}$. Increasing $\Delta\rho_{top}$, the HNB will move to a lower level. For any given K_{S2} and m_α, there is a $\Delta\rho_{top}$ above which $\Delta\rho_{ch}$ is greater than $\Delta\rho_{th}$ for all depths, and another $\Delta\rho_{top}$ below which $\Delta\rho_{ch}$ is less than $\Delta\rho_{th}$ for all depths. Between the two extremes, $\Delta\rho_{ch}$ intersects with $\Delta\rho_{th}$ in the midmantle, and the estimated HNB has a value between 0 and 1. The range of estimated HNBs expands significantly at large K_{S2} or small m_α.

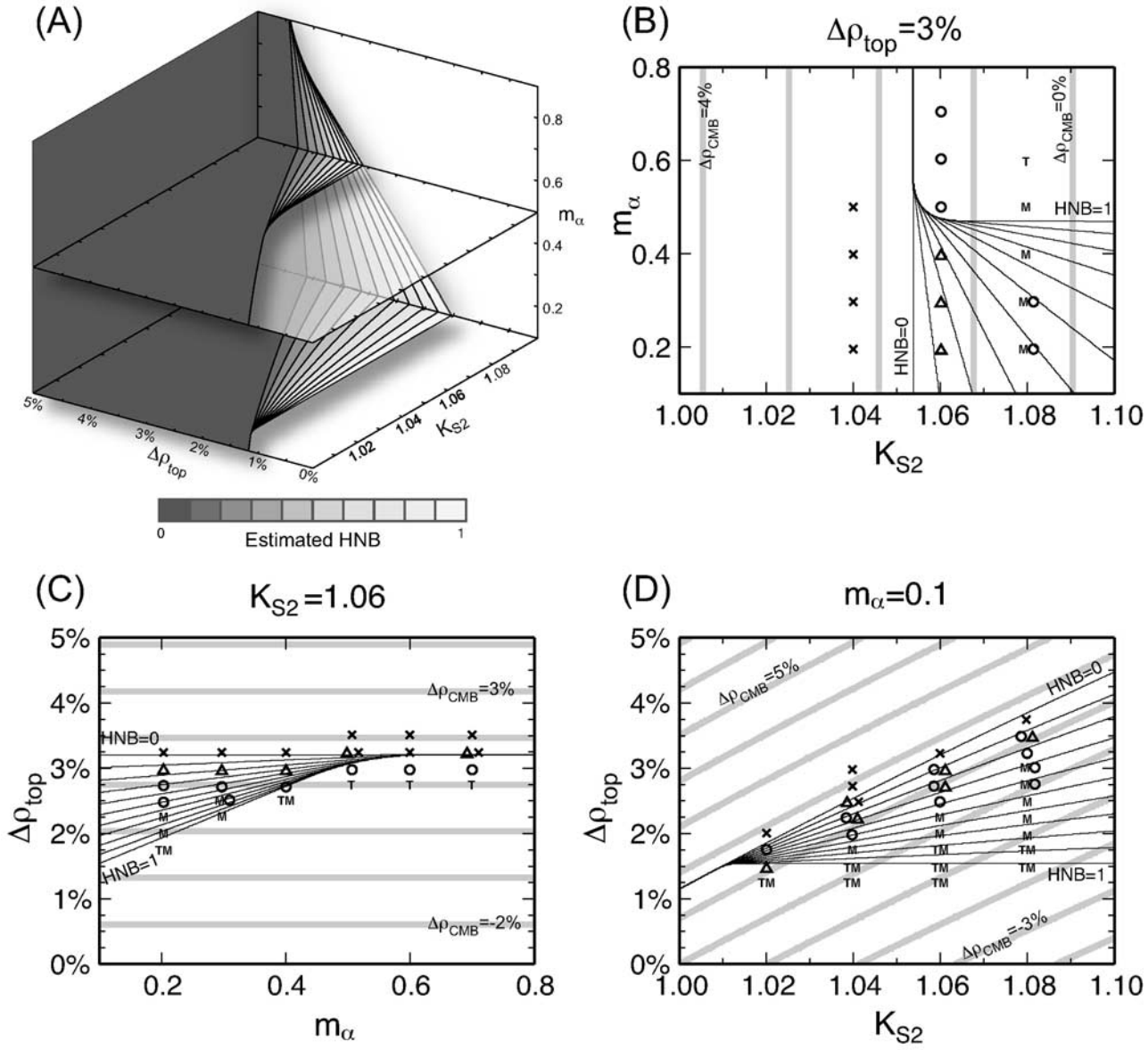

Figure 3. Parameter space. (A) Estimated HNB in the three-dimensional (K_{S2}, $\Delta\rho_{top}$, m_α) parameter space. (B–D) Cross sections of the parameter space. (B) $\Delta\rho_{top}$ = 3% (C) K_{S2} = 1.06; (D) m_α = 0.1. The thin contours are for the estimated HNB with an interval of 0.1. The thick, gray contours are for $\Delta\rho_{CMB}$ with an interval of 1%. The outcomes of models are plotted with symbols. T: classical thermochemical plumes. M: mushroom-shaped plumes. ○: domes. Δ: ridges. ×: continuous layers.

[33] Guided by Figure 3a, 130 numerical thermochemical convection models were calculated, each with distinct values of K_{S2}, $\Delta\rho_{top}$, and m_α. The range of parameter space explored is $1.02 \leq K_{S2} \leq 1.08$, $1.25\% \leq \Delta\rho_{top} \leq 3.75\%$, and $0.1 \leq m_\alpha \leq 0.7$. We find a wide range of thermochemical structures that we categorize in terms of morphology and evolution (Table 3). We calculate $\delta T = \delta T(z)$ by taking the horizontal temperature average in the region of $C > 0.8$ and use δT to infer $\Delta\rho_{th}$. We divide the result into three groups in terms of how the profiles of $\Delta\rho_{th}$ and $\Delta\rho_{ch}$

Table 3. Summary of Converted Seismic Models

Category	Plume	Mushroom	Dome	Ridge	Layer
Preferred parameters	Small $\Delta\rho_{top}$, small K_{S2}, large m_α	Small $\Delta\rho_{top}$, large K_{S2}	Intermediate $\Delta\rho_{top}$ and large m_α	Intermediate $\Delta\rho_{top}$ and small m_α	Large $\Delta\rho_{top}$ and small m_α
δT	Variable	<0.6	0.7	0.8	>0.8
$\Delta\rho$	Very buoyant	Buoyant	Neutral	Neutral	Dense
Stability	Unstable	Unstable	Stable	Stable	Stable
HNB	>d or N/A	>d	>∼d	∼d	<d or N/A

intersect: (1) The profiles never intersect; (2) they intersect and $\Delta\rho_{ch}$ dominates below the intersection; and (3) they intersect and $\Delta\rho_{th}$ dominates below the intersection. Within each group, two or more categories of evolution can be found. We will present one model in each category, showing temperature, composition, and density fields, and will describe the dynamic evolution of each.

3.1 No Intersection

[34] When the profiles of $\Delta\rho_{th}$ and $\Delta\rho_{ch}$ never intersect, two outcomes exist. If $\Delta\rho_{th}$ is always greater than $\Delta\rho_{ch}$, a small temperature increase in the chemical layer is sufficient to destabilize it. Several thermochemical plumes form and reach the top of domain. The plume heads impinge the top boundary and spread horizontally. All of the anomalous material is entrained into the plumes and transported to the top of the domain. The plumes have highly variable δT (Figure 4a). We call this category "classical thermochemical plumes" and label it "T" in Figure 3, mimicking the shapes of plume conduits and spreading plume heads. This category occurs at small $\Delta\rho_{top}$ and K_{S2} or at large m_α. This category should be very common at the parameter space of small $\Delta\rho_{top}$ and K_{S2} but is underrepresented in our sampling of the parameter space. There are a few models of large K_S, and m_α also produce classical thermochemical plumes. The early evolution of these models is similar to the evolution of models of "mushroom-shaped plumes" (described below). However, the large m_α in these models controls whether the plumes eventually rise to the surface.

[35] On the other hand, if $\Delta\rho_{th}$ is always smaller than $\Delta\rho_{ch}$, the anomalous material forms a hot, continuous layer with δT greater than 0.8. The layer interface has small topography. Thermal plumes rising above the layer entrain small amounts of anomalous material. Sharp cusps of the layer interface occur at the roots of thermal plumes (Figure 4b). We call this category "continuous layer" and label it with a cross ($\times$) in Figure 3. This category occurs at large $\Delta\rho_{top}$ and small m_α.

3.2. $\Delta\rho_{ch}$ Dominates Below the Intersection

[36] When $\Delta\rho_{ch}$ dominates $\Delta\rho_{th}$ below the intersection, depending on the height of intersection, there are mainly two kinds of structures. First, if the height of intersection is low and close to the CMB, the whole layer can erupt as a plume, like the "classical thermochemical plumes" category above. Second, if the height of intersection is sufficiently high, such that the anomalous material never rises to this level, the layer remains at the CMB, akin to the "continuous layer" category.

3.3. $\Delta\rho_{th}$ Dominates Below the Intersection

[37] When $\Delta\rho_{th}$ dominates over $\Delta\rho_{ch}$ below the intersection, the height of intersection is the HNB. A broad range of dynamic evolutionary sequences can be found, depending on HNB and the magnitude of $\Delta\rho_{ch}$ at the CMB, $\Delta\rho_{CMB}$. If HNB is near the top of the computational domain, the whole layer can erupt as a plume, like the "classical thermochemical plumes" category. If HNB is near the CMB, the whole layer remains near the CMB, like the "continuous layer" category. In the intermediate range of HNB, three typical states exist, which will be described below.

[38] The first category is the "mushroom-shaped plume" (Figure 4c). In this category, the HNB is significantly higher than the initial thickness of the chemical layer d, and $\Delta\rho_{CMB}$ is small, typically less than 0.8%. Several thermochemical plumes form with δT usually less than 0.6. Unlike the classical thermochemical plumes, the bulk of the mushroom-shaped plumes never reach to the top of the domain. The head of a mushroom-shaped plume entrains cold material during its ascent. Subsequently, some of the cold material in the plume head starts to descend in the midmantle, forming dripping side lobes. Simultaneously, the plume conduit continues to bring warm material into the rising plume conduit. All of the anomalous material is entrained in the plumes. Although a small amount of anomalous material with exceptionally high temperature reaches the top boundary, most of the anomalous material reaches the midmantle. The dripping side lobes and rising conduit together have a mushroom shape. This category is labeled "M" in Figure 3. This category occurs at the combination of small $\Delta\rho_{top}$ and large K_{S2}.

[39] The second category is the "dome" (Figure 4d). In this category, the HNB is higher than d, and $\Delta\rho_{CMB}$ is between 0.8% and 1.2%. Small-scale convection first develops within the chemical layer, but eventually several small convection cells coalesce into a few large cells. The coalesced convection cells are well separated from each other. The size of the convection cells continues growing until they reach the HNB, where the positive density anomaly caps their tops. The domes are rounded or flat-topped with very steep sidewalls. The bulk of the anomalous material remains confined to the domes. The thermal plumes, developed on the top of the domes, entrain only a small fraction of the anomalous material. δT of the dome is about 0.7, agreeing with the temperature upon which the HNB was estimated in Figure 3. This category is labeled with circles () in Figure 3. This category occurs at intermediate $\Delta\rho_{top}$ and prefers larger m_α.

[40] The third category is the "ridge" (Figure 4e). The HNB is lower than but close to d, and $\Delta\rho_{CMB}$ is between 1.2% and 1.8%. The evolution is similar to the "dome" category above. However, the structure is like a triangular ridge, with gentle-sloping sidewalls. The temperature of the ridges is uniform with δT greater than 0.7. This category is labeled with triangles (Δ) in Figure 3. This category occurs at intermediate $\Delta\rho_{top}$ and prefers smaller m_α.

[41] The distinction between these three later categories deserves detailed analysis. When the HNB is significantly higher than d, model outcomes will fall in either the mushroom or the dome category, depending on the magnitude of $\Delta\rho_{CMB}$. If $\Delta\rho_{CMB}$ is less than 0.8%, a small temperature increase is sufficient to destabilize the layer. Short-wavelength instability within the chemical layer grows quickly and detaches from the bottom, forming several small plumes with small δT. On the other hand, if $\Delta\rho_{CMB}$ is greater than 0.8%, a large temperature increase is required to destabilize the layer. Instabilities at short wavelengths within the chemical layer merge, forming long wavelength structures, so that the layer further accumulates heat. This leads to larger domes compared to detached mushroom-shaped plumes.

[42] When the HNB is comparable to d, the chemical structure of the model outcome will be either a dome or a ridge. If $\Delta\rho_{CMB}$ is less than 1.2%, the base of the structure is buoyant. Strong active upwellings inside the structure rise along the sidewalls. The buoyancy of the upwellings maintains the steep sidewalls, forming a dome. On the other

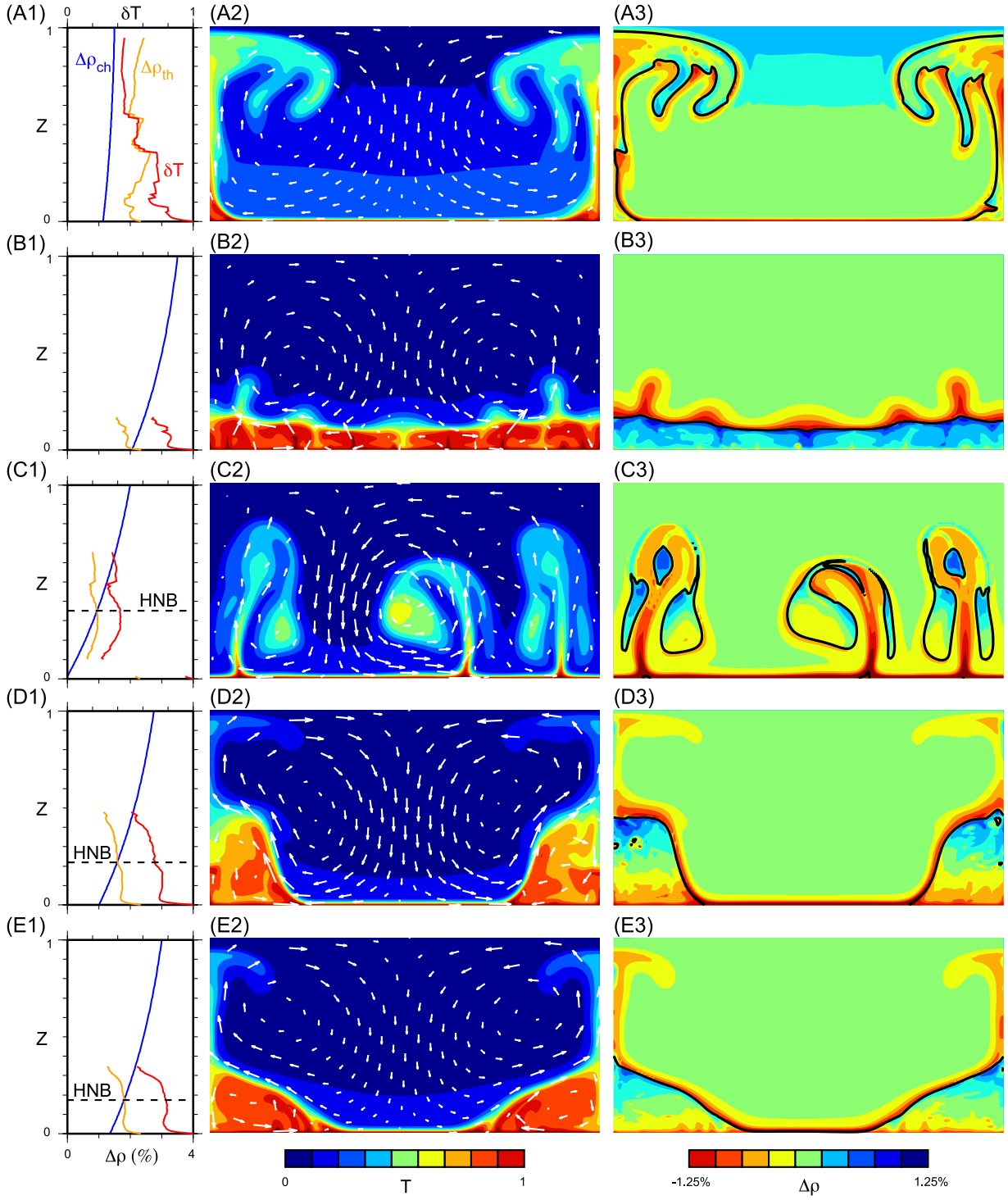

Figure 4. Results of various models. The left column shows the profiles of $\Delta\rho_{ch}$, $\Delta\rho_{th}$, and δT. The central column shows the temperature and velocity field. The right column shows the density and composition field. The black line is the contour of $C = 0.5$. (A1–3) Classical thermochemical plume. $K_{S2} = 1.02$. $\Delta\rho_{top} = 1.5\%$. $m_\alpha = 0.7$. (B1–3) Continuous layer. $K_{S2} = 1.06$. $\Delta\rho_{top} = 3.5\%$. $m_\alpha = 0.1$. (C1–3) Mushroom-shaped plume. $K_{S2} = 1.06$. $\Delta\rho_{top} = 2\%$. $m_\alpha = 0.1$. (D1–3) Dome. $K_{S2} = 1.06$. $\Delta\rho_{top} = 2.75\%$. $m_\alpha = 0.1$. (E1–3) Ridge. $K_{S2} = 1.06$. $\Delta\rho_{top} = 3\%$. $m_\alpha = 0.1$.

hand, if $\Delta\rho_{CMB}$ is greater than 1.2%, $\Delta\rho_{ch}$ is close to $\Delta\rho_{th}$. The net density anomaly is small, and the buoyancy force is less important in controlling the shape of the structure. Instead, the shape of the structure is controlled by the viscous stress of the background flow. The background flow near the CMB pushes the structure into a triangular ridge. The magnitude of density heterogeneity inside a ridge is significantly less than that inside a dome.

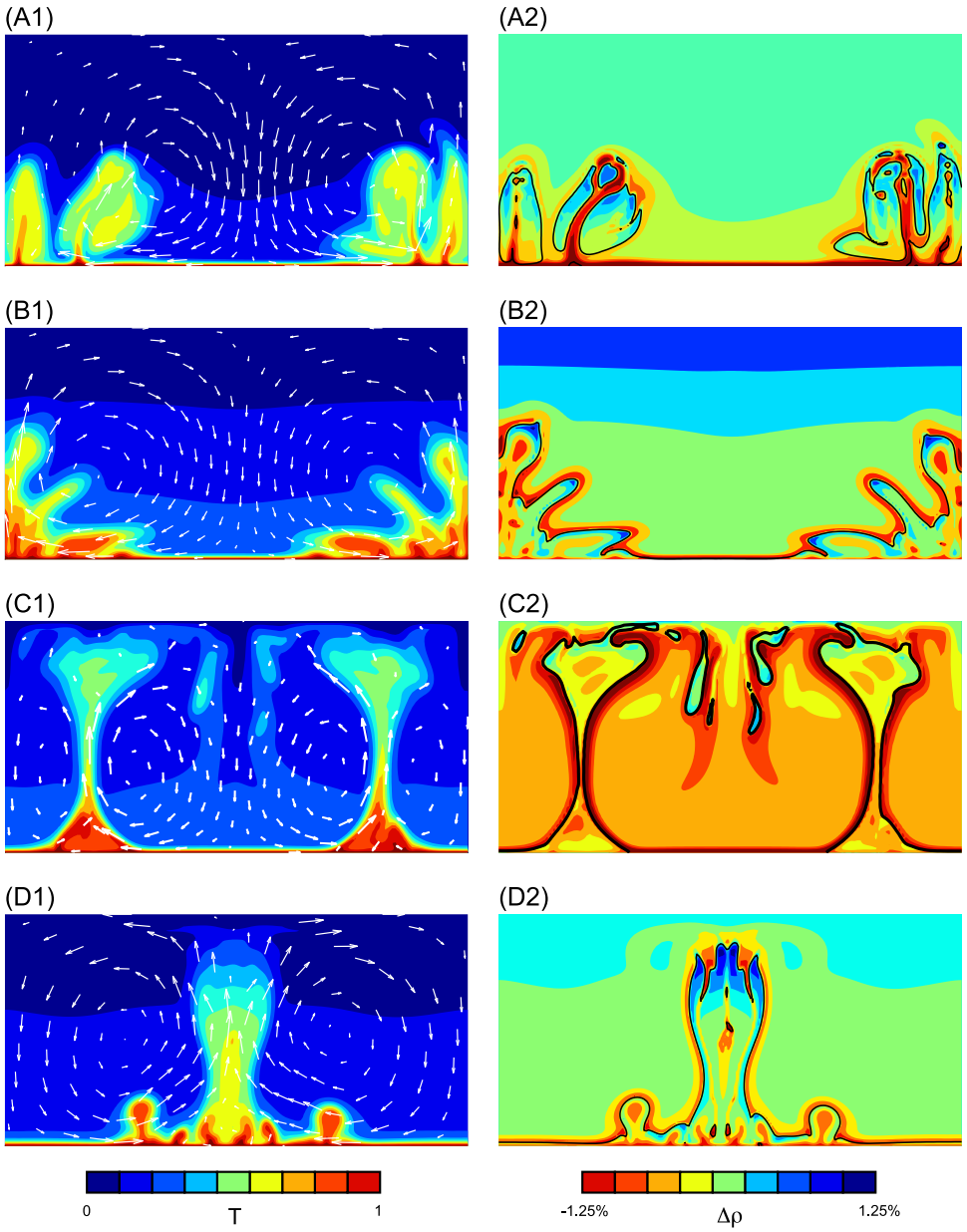

Figure 5. Additional model outcomes. (A) Mushroom-shaped plumes swept into piles. K_{S2} = 1.08. $\Delta\rho_{top}$ = 3%. m_α = 0.2. (B) Early stage of a classical thermochemical plume. K_{S2} = 1.02. $\Delta\rho_{top}$ = 1.5%. m_α = 0.7. (C) Hourglass-shaped plume. K_{S2} = 1.02. $\Delta\rho_{top}$ = 1.75%. m_α = 0.7. (D) Columnar plume. K_{S2} = 1.02. $\Delta\rho_{top}$ = 1.5%. m_α = 0.5.

[43] A model with identical parameters as in Figure 4d is calculated in a 6 × 1 box. The results are similar to Figure 4d, except that there are four domes in the box. The four domes are evenly spaced horizontally, with two of them on the edges of the box. The domes all have similar heights and amounts of entrainment. This suggests that the morphology of the chemical structures is not affected by the aspect ratio of the box.

3.4. Remarks

[44] The division between the five categories is gradual and not sharp. A chemical structure can exhibit morphology akin to two categories. For a model at the transition between the classical thermochemical plume and the mushroom-shaped plume, part of the plume head forms dripping side lobes that fall, while the other part of the plume head impinges the top boundary. For a model at the transition between the mushroom-shaped plume and the dome, the dripping side lobes of various plumes are swept by the background flow and merge, forming a large dome (Figure 5a). For a model at the transition between the dome and ridge, its shape is between that of a triangular ridge and a rounded dome. For a model at the transition between the ridge and the continuous layer, the bases of the ridges interconnect. These transitional models are labeled as double symbols in Figure 3.

[45] We must emphasize the importance of presenting the density field for discerning the dynamics of thermochemical convection. Chemical structures with different evolutionary

pathways can exhibit similar morphologies at a single time; temperature alone cannot predict subsequent evolution. Such ambiguity is removed by showing the density field, which directly relates to the driving force of convection. For example, a classical thermochemical plume at its early stage can resemble a dome in morphology (Figure 5b), but the density field clearly reveals its buoyant nature.

[46] The five categories cover most model outcomes. However, there were a few models that did not fit within the five categories. One example is the "hourglass-shaped plume" (Figure 5c). The profiles of $\Delta\rho_{th}$ and $\Delta\rho_{ch}$ intersect at the midmantle. Below the intersection point, $\Delta\rho_{ch}$ dominates over $\Delta\rho_{th}$, and the anomalous material is stable. But occasionally parcels of anomalous material can rise above the intersection point, where $\Delta\rho_{th}$ dominates. The parcel will rise to the top of the computational domain as a plume. The base of the anomalous material remains at the bottom. The shape of the detached plume and remaining base is similar in appearance to an hourglass, with a narrow "neck" in the midmantle, similar to the structure in Figure 1a. Another example is the "columnar plume" (Figure 5d). The profiles of $\Delta\rho_{th}$ and $\Delta\rho_{ch}$ are subparallel. The anomalous material accumulates into a pile and coherently rises as a column slowly. There might be an HNB, but the dense material above the HNB could not stabilize the column. The column can reach the top of the convection box. Unlike a classical thermochemical plume, a columnar plume has a broad plume conduit and no plume head.

[47] The occurrences of hourglass-shaped and columnar plumes are rare and isolated in the parameter space. Of the 130 cases explored, only one hourglass-shaped and three columnar plumes were found. *Farnetani and Samuel* [2005] found similar types of plumes, but they did not mention how frequently these structures occurred. Because of their restricted range in the parameter space, the significance of hourglass-shaped and columnar plumes in the context of the Earth's mantle is questionable. In contrast, each of the five categories (classical thermochemical plumes, mushroom-shaped plumes, domes, ridges, and continuous layers) spans a well-defined and significant range in the parameter space. As a result, we will concentrate our attention on these five categories in section 4.

[48] Regarding stability, the chemical layers in the classical thermochemical and mushroom-shaped plume categories are unstable, and the bulk of the layer is lifted off the CMB in a few overturn cycles. The chemical layer in the continuous layer category is clearly stable, as the layer will stay at the CMB indefinitely. The dome and ridge are stable too. Although these structures have a high relief, they are never removed from the CMB.

4. Discussion

[49] We have explored a wide range of parameters for compressible thermochemical convection. Now we will apply these results to the Earth's mantle. α_m for the lower mantle material is likely not large, suggesting that an HNB could exist for a wide range of K_{S2} and $\Delta\rho_{top}$. If materials with different K_{S2} and $\Delta\rho_{top}$ exist in the lower mantle, what kind of structures will they form?

4.1. Possible Chemical Structures in the Lower Mantle

[50] Anomalous material with small $\Delta\rho_{top}$ is unstable and will erupt as classical thermochemical plumes or as mushroom-shaped plumes. In both scenarios, the material will mix with the ambient mantle rapidly. The anomalous material is not expected to remain and accumulate at the CMB. As a result, this type of material is not likely to form large-scale structures within the present-day lower mantle. Nevertheless, it is possible for the material to form large-scale structures beneath cold slabs. If the material could somehow accumulate beneath the slabs, the dense and highly viscous slabs will inhibit the boundary layer instability, and a large volume of the anomalous material could accumulate, similar to the results of purely thermal convection models [*Tan et al.*, 2002].

[51] Anomalous material with large $\Delta\rho_{top}$ will form a continuous layer at the base of the mantle. Since a global chemical layer thicker than 100 km has not been found seismologically, this scenario is ignored in this manuscript. However, subducted slabs can impinge and deflect the layer, such that the layer becomes isolated piles [e.g., *McNamara and Zhong*, 2005]. Such "piles" are passive structures, as the high topography of the sidewalls is maintained by slab push. The piles are denser than the ambient mantle but less dense than surrounding slabs. This pattern of density variation will be an important diagnostic. This type of structures is referred to as "passive piles" in later discussion.

[52] Anomalous material with moderate $\Delta\rho_{top}$ will form domes or ridges. Such structures are stable and can remain at the CMB for long periods of geological time. If this type of material exists in a large quantity, we would expect to find domes and ridges in the lower mantle. There is no definitive seismic evidence of ridges, although the part of the African LVS under the Atlantic mid-ocean ridge is a possible candidate. On the other hand, the shape of the dome resembles the shape of the southern part of the African LVS, a broad structure with steep sidewalls and high relief [*Ni and Helmberger*, 2003a, 2003b, 2003c]. Before we can attribute the dome as the dynamic explanation of the southern African LVS, we must address the problem of uniqueness.

4.2. Possible Dynamical Scenarios for LVSs

[53] Several dynamical scenarios have been proposed for LVSs (Figure 6) including the following: (A) buoyant active upwellings [*Forte and Mitrovica*, 2001; *Ni et al.*, 2002]; (B) plume clusters [*Schubert et al.*, 2004]; (C) ridges [*Jellinek and Manga*, 2002; *Tackley*, 2002]; (D) passive piles [*Kellogg et al.*, 1999; *McNamara and Zhong*, 2005]; (E) sluggish domes [*Davaille*, 1999; *McNamara and Zhong*, 2004]; and (F) high-bulk-modulus domes [*Tan and Gurnis*, 2005]. We will introduce each scenario briefly in the following.

[54] Scenario A is similar to the early stage of our classical thermochemical plume model (Figure 5b), where a large, buoyant plume rises to the surface. Scenario B is similar to our model of mushroom-shaped plumes swept together (Figure 5a), where several small plumes are swept together by background flow. Scenarios C and F are described previously in section 3.3 (Figures 4d and 4e). Scenario D is also discussed previously in section 4.1, where a continuous chemical layer is impinged and pushed aside by subducted slabs and becomes an isolated pile. Such piles are passive structures. In scenario E, the dome is more viscous than surrounding mantle and can rise and fall for several overturns. Because of its high viscosity, the particle

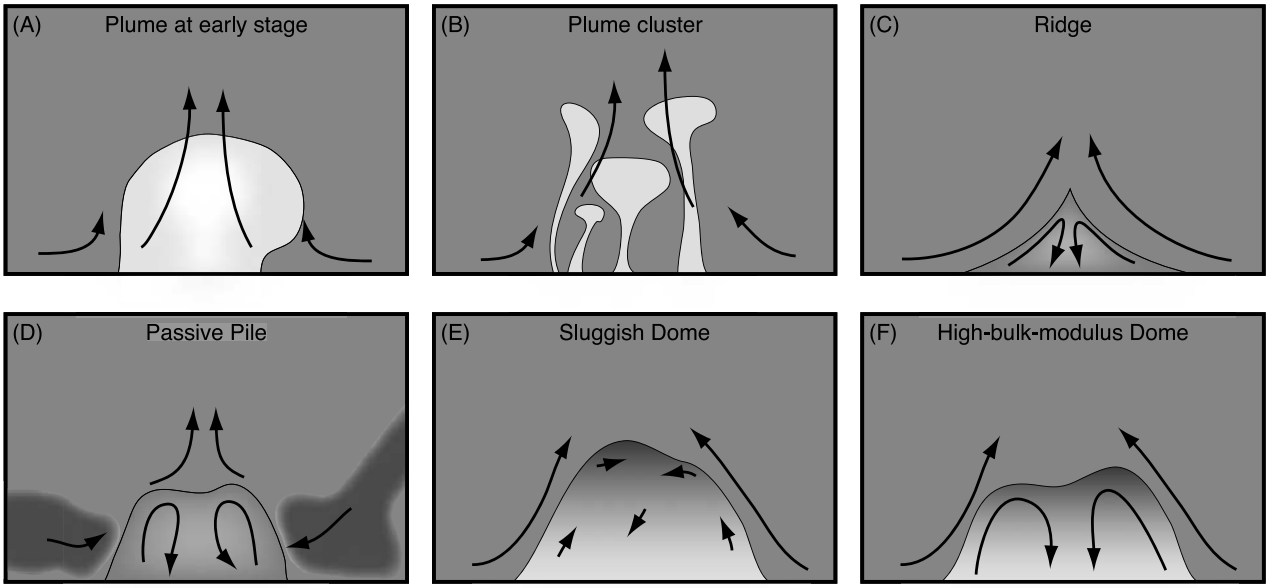

Figure 6. Various dynamic scenarios for LVSs. The gray scale indicates the density anomaly. Darker is denser. The arrows indicate the direction and speed of the flow.

velocity inside the dome is sluggish. This scenario is explored in more detail in another study [*Tan*, 2006, Chapter 7].

[55] In scenario C, the triangular shape of the ridge is distinctive from dome-like structures in other scenarios. A ridge-like structure, when fitted to the resolution of tomography models, is indistinguishable from a dome-like structure [*Tackley*, 2002]. However, the morphology of the southern African LVS is constrained by body wave seismology, which locally has higher resolution than tomography. The seismic observations clearly require a steep sidewall for the southern African LVS. Therefore we reject this scenario for the LVS.

[56] In scenario D, subducted slabs surround the passive pile. As discussed in section 4.1, the piles are denser than ambient mantle but less dense than surrounding slabs. As a result, the pile will look like a low-density anomaly if the horizontal average of density is removed. This is incompatible with results of normal mode inversion [*Ishii and Tromp*, 1999, 2004; *Resovsky and Trampert*, 2003]. However, the veracity of the normal mode inversion is debated, and we cannot rule this scenario out completely.

[57] In the remaining four scenarios, the outline of the chemical structures all have a similar dome shape. With morphology alone, we cannot determine which scenario would represent the southern African LVS best. Fortunately, the southern African LVS has a distinctive seismic velocity anomaly. The southern African LVS has average $\delta V_P = -0.5\%$ and $\delta V_S = -3\%$ [*Ni and Helmberger*, 2003b, 2003c]. Can these dynamic scenarios fit the seismic observation, and, if so, what ranges of thermoelastic parameters are required?

4.3. Conversion to Seismic Anomalies

[58] We transform dynamic model results into seismic velocity anomalies δV_P and δV_S as follows. We assume that the ratio of shear modulus G to bulk modulus K_S, $R_1 = G/K_S$, is fixed at 0.45, similar to PREM at 2700-km depth. The value of R_1 does not strongly affect later analysis. The perturbations to V_P and V_S can be written as

$$\begin{aligned}\delta V_P &= \frac{1}{2}\left(\delta\left(K_S + \frac{4}{3}G\right) - \delta\rho\right)\\ &= \frac{1}{2}\left(\frac{K_S + 4G/3}{K_S + 4G/3} - \delta\rho\right)\\ &= \frac{1}{2}\left(\frac{K_S}{(1+4R_1/3)K_S} + \frac{4R_1G/3}{(1+4R_1/3)G} - \delta\rho\right)\\ &= \frac{1}{2}\left(\frac{\delta K_S + 4R_1\delta G/3}{1+4R_1/3} - \delta\rho\right)\end{aligned} \tag{14}$$

$$\delta V_S = \frac{1}{2}(\delta G - \delta\rho) \tag{15}$$

where ΔK_S and ΔG are the changes in the bulk and shear moduli; $\delta\rho$, δK_S, and δG are the relative perturbations to the density, bulk modulus, and shear modulus, respectively. $\delta\rho$ can be directly retrieved from dynamic models. In average, $\delta\rho$ is in the ranges of -1% to 1%. A simple calculation indicates the required elastic modulus perturbations (Table 4). It is clear that a positive δK_S (i.e., $K_{S2} > 1$) is required by seismic data.

[59] The perturbations to the elastic moduli are decomposed into compositional and thermal parts. Assuming these two parts are linearly independent, we can write

$$\delta K_S = \frac{\partial \ln K_S}{\partial C} C + \frac{\partial \ln K_S}{\partial T}\delta T \tag{16}$$

Table 4. Estimate on Elastic Moduli Perturbation

$\delta\rho$, %	−1	0	1
δK_S, %	1	2	3
δG, %	−7	−6	−5

Table 5. Estimate on Temperature and Composition Derivatives of Elastic Moduli

K_{S2}		1.02			1.04			1.06			1.08		
Average $\delta\rho$, %		−1	0	1	−1	0	1	−1	0	1	−1	0	1
$\delta T\partial\ln K_S/\partial T$, %		−1	0	1	−3	−2	−1	−5	−4	−3	−7	−6	−5
$R_2 = 2.2$	$\delta T\partial\ln G/\partial T$, %	−2.2	0	2.2	−6.6	−4.4	−2.2	−11	−8.8	−6.6	−15.4	−13.2	−11
	$\partial\ln G/\partial C$, %	−4.8	−6	−7.2	−0.4	−1.6	−2.8	4	2.8	1.6	8.4	7.2	6
$R_2 = 2.6$	$\delta T\partial\ln G/\partial T$, %	−2.6	0	2.6	−7.8	−5.2	−2.6	−13	−10.4	−7.8	−18.2	−15.6	−13
	$\partial\ln G/\partial C$, %	−4.4	−6	−7.6	0.8	−0.8	−2.4	6	4.4	2.8	11.2	9.6	8
$R_2 = 3.0$	$\delta T\partial\ln G/\partial T$, %	−3	0	3	−9	−6	−3	−15	−12	−9	−21	−18	−15
	$\partial\ln G/\partial C$, %	−4	−6	−8	2	0	−2	8	6	4	14	12	10

$$\delta G = \frac{\partial \ln G}{\partial C} C + \frac{\partial \ln G}{\partial T} \delta T \tag{17}$$

In the equations above, we used the fact that C is always between 0 and 1. There are four parameters for the composition and temperature derivatives of the elastic moduli. Most of the temperature variation occurs inside material 2. Therefore the temperature derivatives of the elastic moduli of material 1 are unimportant, with the exception in the thermal boundary layer. We will assume that the two materials have the same temperature derivatives of the elastic moduli. The composition derivative of K_S is known.

$$\frac{\partial \ln K_S}{\partial C} = \frac{K_{S2} - K_{S1}}{K_{S1}} = K_{S2} - 1 \tag{18}$$

Furthermore, we assume that the ratio of temperature derivatives of the elastic moduli is constant.

$$\frac{\partial \ln G}{\partial T} \Big/ \frac{\partial \ln K_S}{\partial T} = R_2 \tag{19}$$

R_2 is usually set to 2.6, similar to $MgSiO_3$ perovskite at 2000-km depth between 1500 and 3500 K [*Oganov et al.*, 2001], but sometimes to 2.2 or 3.0.

[60] As a result, two unknown parameters ($\partial\ln G/\partial C$ and $\partial\ln K_S/\partial T$) can be chosen to satisfy the two constraints (average δV_P and δV_S). For any given $\partial\ln K_S/\partial C$ and $\delta\rho$, without knowledge of δT, we can find a unique set of $\delta T\partial\ln K_S/\partial T$, $\delta T\partial\ln G/\partial T$, and $\partial\ln G/\partial C$ that fit the observed average δV_P and δV_S values (Table 5).

[61] In our dynamic models, δT of the anomalous material is usually between 0.6 and 0.8, from which we can estimate $\partial\ln K_S/\partial T$ and $\partial\ln G/\partial T$. For reference, the dimensional values of $\partial\ln K_S/\partial T$ and $\partial\ln G/\partial T$ for $MgSiO_3$ perovskite are -3.29×10^{-5} and -8.62×10^{-5} K^{-1}, respectively [*Oganov et al.*, 2001]. These values can be nondimensionalized by multiplying ΔT_{total}. The temperature contrast ΔT_{total} across the lower mantle is estimated to be in the range of 1800–2400 K [*Boehler*, 2000] and is 1800 K in our dynamic models. After nondimensionalization, for $MgSiO_3$ perovskite, $\delta T\partial\ln K_S/\partial T$ is between −3.5% and −6.3%, and $\delta T\partial\ln G/\partial T$ is between −9.3% and −16.6%. This estimate has large uncertainty and is only applicable to $MgSiO_3$ perovskite. Nevertheless, it represents a useful reference for plausible lower mantle materials.

[62] From Table 5, the case of $K_{S2} = 1.02$ and the case of $K_{S2} = 1.04$ with $\delta\rho > 0$ require a set of $\delta T\partial\ln K_S/\partial T$ and $\delta T\partial\ln G/\partial T$ whose magnitude is far smaller than that of plausible mantle material. On the other hand, for the case of $K_{S2} = 1.08$, extremely negative $\partial\ln K_S/\partial T$ and $\partial\ln G/\partial T$ would produce excessively negative δV_S (<−6%) in the thermal boundary layer that is incompatible with observations. The excessively negative δV_S can be remedied if we allow $\partial\ln K_S/\partial T$ and $\partial\ln G/\partial T$ of material 1 to be less negative than material 2, which is certainly possible. In addition to satisfying average δV_P and δV_S, each of the converted seismic models has additional distinct features contained within the lateral δV_P and δV_S variations, which can also be compared to seismic observation.

[63] Models of classical thermochemical plumes typically occur at small K_{S2} and $\Delta\rho_{top}$. The plume before eruption resembles a dome (scenario A). The high temperature and low density of the "dome" make it difficult to fit the observed average δV_P and δV_S. To fit δV_P, a small negative $\partial\ln K_S/\partial T$ is required, which in turn implies a small negative $\partial\ln G/\partial T$. As argued above, the small magnitude of $\partial\ln K_S/\partial T$ and $\partial\ln G/\partial T$ does not match the thermoelastic property of plausible lower mantle material. We conclude that this scenario is unfavorable. There are a few models of large K_S and m_α that produce classical thermochemical plumes (Figure 3). The early evolution of these models is similar to the evolution of models of mushroom-shaped plume swept together. The seismic signature of these models is discussed below.

[64] For models of mushroom-shaped plumes swept together (scenario B), the vertical plume conduits produce strong lateral temperature and seismic velocity variations (Figure 7a). The plume conduits, made of ambient material, have low δV_S. The dripping side lobes, made of anomalous material, have moderately low δV_S. Such vertical layering should be easily visible by seismic waves traveling vertically through the structure, like SKS or PKP. The southern African LVS is well sampled by SKS. But no internal vertical layering is found [*Ni and Helmberger*, 2003a]. Therefore we reject this scenario as an explanation of the LVS.

[65] The scenario of sluggish domes is explored in another study [*Tan*, 2006, Chapter 7]. The results are summarized here. Because of its high viscosity, the particle motion inside the dome is sluggish. The sluggish motion inside the dome allows effective cooling and inefficient mixing. As a result, a strong temperature gradient develops inside the dome. The base of the dome is warmer and less dense than the crest. The strong temperature and density gradients consequently produce strong vertical gradients in δV_S and δV_P. However, the δV_S and δV_P of the southern African LVS appear to be vertically uniform from S and

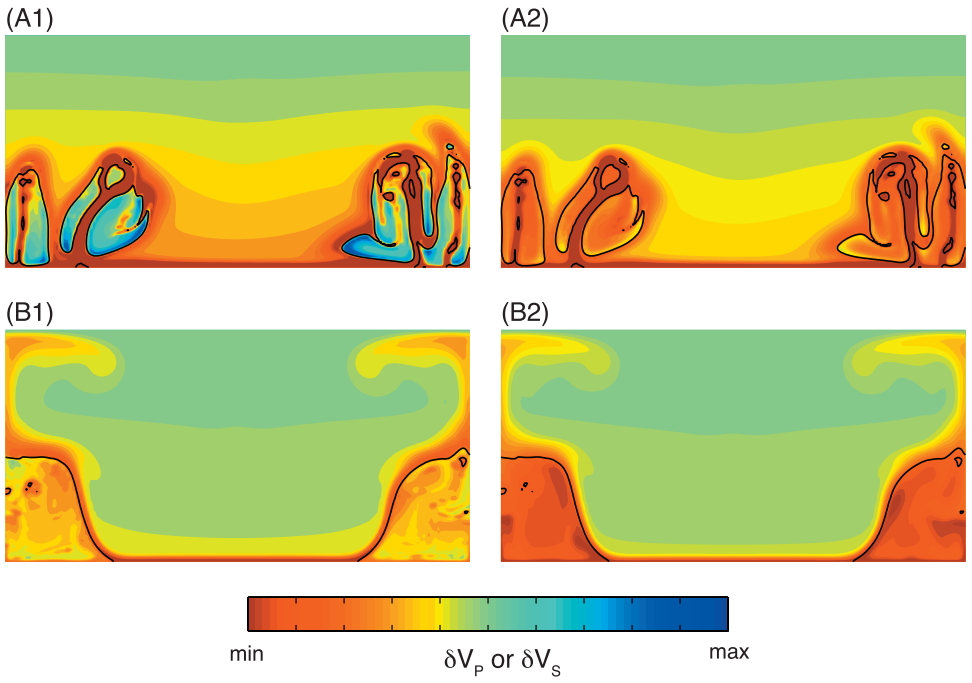

Figure 7. Predicted seismic anomalies. δV_P is displayed on the left column (−1.5% to 1.5%), and δV_S on the right (−4% to 4%). (A) Converted from Figure 5a, using $R_2 = 2.6$, $\partial \ln K_S/\partial T = -8\%$, and $\partial \ln G/\partial C = 7\%$. (B) Converted from Figure 4d, using $R_2 = 2.6$, $\partial \ln K_S/\partial T = -6\%$, and $\partial \ln G/\partial C = 4.4\%$.

S_CS sampling [*Sun et al.*, 2007]. Therefore we reject the scenario.

[66] For models of high-bulk-modulus domes, the thermal boundary layer outside the chemical boundary produces a δV_P minimum. In contrast, δV_S smoothly decreases across the thermal boundary layer and has a local minimum at the inner edge of the chemical boundary (Figure 7b). The minimum of δV_S and δV_P is offset in a horizontal profile. Such an offset is found in all models of high-bulk-modulus domes. The converted seismic model fits the observation surprisingly well. The converted seismic model fits not only the average δV_S and δV_P, but also traveltimes versus epicenter distance for S, S_{diff}, S_CS, SKS, P, P_{diff}, P_CP, and PKP phases [*Sun et al.*, 2007]. Furthermore, the thermoelastic parameters required by the fit are close to the parameters of $MgSiO_3$ perovskite [*Oganov et al.*, 2001]. Therefore the high-bulk-modulus dome scenario is favored as an explanation of the southern African LVS. Finally, the density structure, close to neutral buoyancy predicted by the model, is compatible with dynamic flow models that simultaneously match observed topography and uplift rate of the African LVS [*Gurnis et al.*, 2000].

[67] Because of entrainment, the chemical structure will gradually lose its density contrast and adjust its morphology accordingly. For example, a continuous layer can evolve into a ridge and then to a high-bulk-modulus dome over geological timescales. As a result, a continuum of morphologies is expected in the mantle [*Davaille et al.*, 2005]. We suspect that the mid-Atlantic African LVS is an elongated ridge structure. As its density decreases by entrainment, the LVS becomes a high-bulk-modulus dome structure in the southern part. Our interpretation is similar to that of *Davaille et al.* [2005], except that they invoke a highly viscous layer (sluggish dome) to explain the dome-like structures.

4.4. Implication to Geochemistry and Mineralogy

[68] Hot spot volcanism is common above mantle LVSs. If mantle plumes originate from the LVSs, they must carry entrained LVS material. LVSs can be the source reservoir of the DUPAL (Dup, Dupre; Al, Allegre) anomaly [*Castillo*, 1988], and thermal plumes rising on top of the LVSs can slowly entrain the anomalous material. The DUPAL anomaly has high Pb^{207}/Pb^{204}, Pb^{208}/Pb^{204}, and Sr^{87}/Sr^{86} ratios, indicating that the source reservoir is enriched in U, Th, and Rb. The isotopic age of the source reservoir of the DUPAL anomaly is estimated to be 1–2 Gyrs [*Hofmann*, 1997]. Only the high-bulk-modulus structures (domes and ridges) and the stable continuous layer can survive for such a long time.

[69] A popular hypothesis for the material of the source reservoir is that it is a recycled material that was once fractionated (for example, oceanic crust or enriched oceanic lithosphere) and later subducted back into the deep mantle [*Hofmann and White*, 1982; *Hirschmann et al.*, 2003]. Pyroxenite is a pyroxene-rich ($MgSiO_3$) rock that lacks sufficient olivine (Mg_2SiO_4) to be considered peridotitic. Pyroxenite is commonly attributed to recycled oceanic crust [*Hauri*, 1996] or enriched oceanic lithosphere [*Hirschmann et al.*, 2003]. In the lower mantle, a pyroxenite will contain more perovskite ($MgSiO_3$) and less magnesiowüstite (MgO) than the peridotitic mantle. Because the perovskite is denser and less compressible than the magnesiowüstite, pyroxenite will be denser and will have a higher bulk modulus than the peridotitic mantle. In fact, pyroxenite has been shown to be

1–2% denser and have a 7% higher bulk modulus than PREM for a 1600-K adiabat [*Lee et al.*, 2005], which is consistent with the material properties of a high-bulk-modulus dome. Fe enrichment might be required to increase the density of pyroxenite to better match the dynamic models. Recent mineralogical inversion of seismic data suggests that the LVSs are enriched in perovskite and Fe [*Trampert et al.*, 2004], which agrees with the pyroxenite model.

[70] The volume of the African LVS has been estimated to be at least 10^{10} km^3 [*Ni and Helmberger*, 2003c]. The volume of the Pacific LVS is possibly smaller, and we assume that it is about 5×10^9 km^3. So the total volume of the LVSs is about 1.5×10^{10} km^3. The average thickness of oceanic crust is 7 km, and the subduction rate of oceanic crust is about 20 km^3/yr. From a simple mass balance calculation, the replenishment time of LVSs by oceanic crust is about 0.75 Gyrs, which is consistent with the longevity of high-bulk-modulus domes in the dynamic model. In the mass balance calculation, we assumed that all subducted oceanic crust goes into LVSs, which is unlikely. Some of the subducted oceanic crust may not segregate from the subducted lithosphere and mix with the mantle [*Christensen and Hofmann*, 1994]. Therefore the replenish time of 0.75 Gyrs is a lower bound of the age of the LVSs. The actual age can easily be 1 Gyrs or older, which would reconcile with the observed isotopic age.

5. Conclusion

[71] The anticorrelation of δV_S and δV_P in the LVSs suggests that the material in LVSs have a higher K_S than ambient material. Using composition-dependent compressibility and a density difference between chemical compositions at a reference pressure, a composition-dependent density profile is derived. Together with depth-dependent thermal expansion, this combination of parameters yields a wide range of dynamic evolutions for the chemical layer. The chemical structures are classified in five major categories, classical plumes, mushroom-shaped plume, domes, ridges, and continuous layers, and a few abnormal cases, such as hourglass-shaped plumes and columnar plumes. Several models have a chemical structure morphologically similar to the southern African LVS, at least at a single time.

[72] Guided by our models, several dynamic scenarios are proposed for the dynamic nature of the LVSs, including plumes at an evolutionary early stage, plume clusters, ridges, passive piles, sluggish domes, and high-bulk-modulus domes. We convert these dynamic models into seismic velocity anomalies. Plumes at an early stage are too buoyant and require implausible thermoelastic parameters to match the seismic signature of the LVS. Ridges do not have steep sidewalls, as does southern African LVS. Plume clusters have strong horizontal variations in seismic velocity, which is not detected in the southern African LVS. Sluggish domes have strong vertical gradients in seismic velocity, which is not detected in the southern African LVS either. These four scenarios are rejected as an explanation of the southern African LVS. The two scenarios that remain, passive domes and high-bulk-modulus domes, can be distinguished by their density signature. A passive dome is less dense than its surroundings, while a high-bulk-modulus dome is denser than its surroundings. The density anomaly by normal mode inversion suggests that the scenario of bulk-modulus domes is preferred. Moreover, the high-bulk-modulus domes are compatible with perovskite-like thermoelastic parameters.

[73] We conclude that the southern African LVS is likely a high-bulk-modulus dome. We suggest that pyroxenite, a perovskite-rich rock, is the primary constituent of the high-bulk-modulus dome, and also hypothesize a link between subducted mid-ocean ridge basalts (MORB) and the high-bulk-modulus dome.

6. Future Works

[74] In this study, the profile of ρ_r is parameterized by the composition-dependent bulk modulus and hydrostatic compression, and the profile of α is parameterized by a linear equation. The bulk modulus is assumed constant with depth and temperature. This approach does not take the thermodynamics into account. However, it enables us to take into account the effect of the density dependence on hydrostatic pressure, which is the main effect of replacing incompressible with compressible convection. Furthermore, in the conversion to seismic models, we consider the temperature dependence of the bulk modulus, which is inconsistent with the previous assumption. Such inconsistency is shared among current generation of dynamic models. Ideally, the dynamic model should be complemented by an equation of state from mineral physics. Given the temperature, pressure, and composition fields from dynamic models, the equation of the state can be used to calculate the density and elastic moduli, which can be fed back into dynamic models to drive the convection (density) or to predict the seismic velocity (elastic moduli). Such an approach is desirable in modeling the thermochemical evolution of Earth.

Appendix A: Benchmark of Compressible Stokes Flow Solver

[75] We follow a similar procedure to that of *Hager and O'Connell* [1981] to develop an analytical solution for Stokes flow in a compressible, Newtonian fluid.

$$\nabla \cdot (\rho_r \mathbf{u}) = 0 \tag{A1}$$

$$-\nabla P + \nabla \cdot \underline{\tau} = \rho Ra \mathbf{e}_z \tag{A2}$$

[76] If the viscosity variation is restricted in the z direction only, the equation can be decomposed in Fourier series. Without losing generality, the flow is assumed to be periodic with a wave number k in the x direction. The flow variables can be expressed as

$$u_z(x,z) = U_z(z) \cos kx \tag{A3}$$

$$u_x(x,z) = U_x(z) \sin kx \tag{A4}$$

$$\sigma_{zz}(x,z) = \Sigma_{zz}(z)\cos kx \tag{A5}$$

$$\sigma_{xx}(x,z) = \Sigma_{xx}(z)\cos kx \tag{A6}$$

$$\sigma_{xz}(x,z) = \Sigma_{xz}(z)\sin kx \tag{A7}$$

$$P(x,z) = \Pi(z)\cos kx \tag{A8}$$

$$\Delta\rho(x,z) = \Omega(z)\cos kx \tag{A9}$$

where $\sigma = \tau - P\underline{I}$ is the total stress tensor. The reference density profile is assumed to be

$$\rho_r(z) = e^{\beta(1-z)} \tag{A10}$$

where $\beta = Di/\gamma$. Substitution of equations (A3), (A4), and (A10) into the continuity equation (A1) yields

$$\partial U_z = -kU_x + \beta U_z \tag{A11}$$

where ∂ is a shorthand for d/dz.

[77] Similarly, the constitutive relationship, equations (4) and (5), becomes

$$\Sigma_{zz} = \eta\left[\frac{4}{3}\partial U_z - \frac{2}{3}kU_x\right] - P \tag{A12}$$

$$\Sigma_{xx} = \eta\left[-\frac{2}{3}\partial U_z + \frac{4}{3}kU_x\right] - P \tag{A13}$$

$$\Sigma_{xz} = \eta[\partial U_x - kU_z] \tag{A14}$$

The expression for pressure can be obtained by combining equations (A11) and (A12).

$$\Pi = \eta\left[-2kU_x + \frac{4}{3}\beta U_z\right] - \Sigma_{zz} \tag{A15}$$

The expression of Σ_{xx} can be obtained by combining equations (A11)–(A13).

$$\Sigma_{xx} = \Sigma_{zz} - 2\beta\eta U_z + 4k\eta U_x \tag{A16}$$

[78] The Stokes equation (A2) becomes

$$-k\Sigma_{xx} + \partial\Sigma_{xz} = 0 \tag{A17}$$

$$k\Sigma_{xz} + \partial\Sigma_{zz} = \Omega Ra \tag{A18}$$

Table A1. Benchmarks of the Stokes Flow Solver

Approximation	a_n	No. of Elements	Relative Error on u_z, %
BA	0	16	0.374
BA	0	32	0.0937
BA	0	64	0.0234
TALA	0	16	0.366
TALA	0	32	0.0916
TALA	0	64	0.0229
TALA	2	16	0.450
TALA	2	32	0.113
TALA	2	64	0.0281

Substituting equation (A16) into equation (A17) yields

$$\partial\Sigma_{xz} = k\Sigma_{zz} - 2\beta k\eta U_z + 4k^2\eta U_x \tag{A19}$$

Combining equations (A11), (A12), (A18), and (A19), we obtain a set of linear equations

$$\partial\begin{bmatrix} U_z \\ U_x \\ \Sigma_{zz}/2\eta_0 k \\ \Sigma_{xz}/2\eta_0 k \end{bmatrix} = \begin{bmatrix} \beta & -k & 0 & 0 \\ k & 0 & 0 & 2k/\eta^* \\ 0 & 0 & 0 & -k \\ -\beta\eta^* & 2k\eta^* & k & 0 \end{bmatrix} \cdot \begin{bmatrix} U_z \\ U_x \\ \Sigma_{zz}/2\eta_0 k \\ \Sigma_{xz}/2\eta_0 k \end{bmatrix} + \begin{bmatrix} 0 \\ 0 \\ \Omega Ra/2\eta_0 k \\ 0 \end{bmatrix} \tag{A20}$$

where $\eta^* = \eta/\eta_0$, and η_0 is an arbitrary constant. The purpose of η_0 is to dimensionalize the vector on the left-hand side. Note that when $\beta = 0$, there is no adiabatic density gradient, and equation (A20) is reduced to the result of the study by *Hager and O'Connell* [1981]. Subject to free-slip boundary conditions at the top and bottom surface, equation (A20) is a boundary value ordinary differential equation, which can be solved analytically. Instead, we use the *bvp4c* function in MATLAB [*Shampine et al.*, 2003] to solve the equation numerically up to machine precision. The solution obtained is referred to as the "analytical solution" hereinafter.

[79] We compared the finite element solution with the analytical solution. The finite element calculation is computed using 16, 32, or 64 elements in each direction in a unit box. By changing the value of Di and γ, different approximations of the governing equations are benchmarked: Boussinesq approximation (BA, $Di = 0$ and $\gamma = \infty$), extended Boussinesq approximation (EBA, $Di = 0.5$ and $\gamma = \infty$), and truncated anelastic liquid approximation (TALA, $Di = 0.5$ and $\gamma = 1$). The density anomaly is set according to

$$\Delta\rho(x,z) = \rho_r(z)T(x,z) \tag{A21}$$

$$T(x,z) = \sin\pi z\cos kx \tag{A22}$$

The viscosity is $\eta = e^{az}$, where a is either 0 or 2. The error on X is defined as $\mathrm{RMS}(X_{\mathrm{numerical}} - X_{\mathrm{analytical}})/\mathrm{RMS}(X_{\mathrm{analytical}})$,

Table B1. Benchmarks of the Energy Equation Solver

Approximation	a_n	No. of Elements	Relative Error on $\partial T/\partial t$, %
BA	0	16	10.11
BA	0	32	5.20
BA	0	64	3.40
TALA	0	16	9.47
TALA	0	32	4.61
TALA	0	64	2.64
TALA	2	16	8.20
TALA	2	32	3.90
TALA	2	64	1.92

where RMS is the root mean square. The result of the benchmark is in Table A1.

Appendix B: Benchmark of Compressible Temperature Solver

[80] Once the analytical solution of the velocity and stress are obtained, they can be substituted into the energy equation (3). Assuming $C_P = k_T = \alpha = g = 1$, each term of the energy equation can be expressed analytically.

$$-\rho_r \mathbf{u} \cdot \nabla T = e^{\beta(1-z)}\left(kU_x \sin^2 kx \sin \pi z - \pi U_z \cos^2 kx \cos \pi z\right) \tag{B1}$$

$$\nabla \cdot k_T \nabla T = \left(-k^2 - \pi^2\right) \cos kx \sin \pi z \tag{B2}$$

$$Di(T + T_{surf})\rho_r u_z = Die^{\beta(1-z)} U_z \cos kx(\sin \pi z \cos kx + T_s) \tag{B3}$$

$$\frac{Di}{Ra}\underline{\sigma} : \underline{\varepsilon} = \frac{Di}{Ra}\eta\left(4k^2 U_x^2 + \frac{4}{3}\beta^2 U_z^2 - 4\beta k U_x U_z\right) \times \cos^2 kx + \frac{1}{\eta^2_{xz}} \sin^2 kx \tag{B4}$$

$$\rho_r H = e^{\beta(1-z)} H \tag{B5}$$

The result of the benchmark is in Table B1.

[81] **Acknowledgments.** This research has been supported by NSF grants EAR-0205653 and EAR-0215644. We thank Don Helmberger for continuous discussion during the course of this work. This work represents contribution 9165 of the Division of Geological and Planetary Sciences, California Institute of Technology.

References

Akber-Knutson, S., G. Steinle-Neumann, and P. D. Asimow (2005), Effect of Al on the sharpness of the $MgSiO_3$ perovskite to post-perovskite phase transition, *Geophys. Res. Lett.*, *32*, L14303, doi:10.1029/2005GL023192.

Allegre, C. J., O. Brevart, B. Dupre, and J. F. Minster (1980), Isotopic and chemical effects produced in a continuously differentiating convecting earth mantle, *Philos. Trans. R. Soc. London, Ser. A*, *297*, 447–477.

Anderson, O. L. (1967), Equation for thermal expansivity in planetary interiors, *J. Geophys. Res.*, *72*, 3661–3668.

Badro, J., J. P. Rueff, G. Vanko, G. Monaco, G. Fiquet, and F. Guyot (2004), Electronic transitions in perovskite: Possible nonconvecting layers in the lower mantle, *Science*, *305*, 383–386.

Balachandar, S., D. A. Yuen, and D. Reuteler (1992), Time-dependent 3-dimensional compressible convection with depth-dependent properties, *Geophys. Res. Lett.*, *19*, 2247–2250.

Barrett, R., et al. (1994), *Templates for the Solution of Linear Systems: Building Blocks for Iterative Methods*, 2nd ed., 141 pp., SIAM, Philadelphia, PA.

Baumgardner, J. R. (1985), 3-Dimensional treatment of convective flow in the Earths mantle, *J. Stat. Phys.*, *39*, 501.

Bercovici, D., G. Schubert, and G. A. Glatzmaier (1992), 3-Dimensional convection of an infinite-Prandtl-number compressible fluid in a basally heated spherical-shell, *J. Fluid Mech.*, *239*, 683–719.

Boehler, R. (2000), High-pressure experiments and the phase diagram of lower mantle and core materials, *Rev. Geophys.*, *38*, 221–245.

Brooks, A. N., and T. J. R. Hughes(1982), Streamline upwind Petrov-Galerkin formulations for convection dominated flows with particular emphasis on the incompressible Navier-Stokes equations, *Comput. Methods Appl. Mech. Eng.*, *32*, 199–259.

Brooks, C., S. R. Hart, A. W. Hofmann, and D. E. James (1976), Rb-Sr mantle isochrons from oceanic regions, *Earth Planet. Sci. Lett.*, *32*, 51–61.

Bunge, H. P., M. A. Richards, and J. R. Baumgardner (1997), A sensitivity study of three-dimensional spherical mantle convection at 10^8 Rayleigh number: Effects of depth-dependent viscosity, heating mode, and an endothermic phase change, *J. Geophys. Res.*, *102*, 11,991–12,007.

Burke, K., and T. H. Torsvik (2004), Derivation of large igneous provinces of the past 200 million years from long-term heterogeneities in the deep mantle, *Earth Planet. Sci. Lett.*, *227*, 531–538.

Caracas, R., and R. E. Cohen (2005), Effect of chemistry on the stability and elasticity of the perovskite and post-perovskite phases in the $MgSiO_3$-$FeSiO_3$-Al_2O_3 system and implications for the lowermost mantle, *Geophys. Res. Lett.*, *32*, L16310, doi:10.1029/2005GL023164.

Castillo, P. (1988), The Dupal anomaly as a trace of the upwelling lower mantle, *Nature*, *336*, 667–670.

Castle, J. C., and R. D. van der Hilst (2003), Searching for seismic scattering off mantle interfaces between 800 km and 2000 km depth, *J. Geophys. Res.*, *108*(B2), 2095, doi:10.1029/2001JB000286.

Christensen, U. (1984), Instability of a hot boundary-layer and initiation of thermo-chemical plumes, *Ann. Geophys.*, *2*, 311–319.

Christensen, U. R., and A. W. Hofmann (1994), Segregation of subducted oceanic-crust in the convecting mantle, *J. Geophys. Res.*, *99*, 19,867–19,884.

Davaille, A. (1999), Simultaneous generation of hotspots and superswells by convection in a heterogenous planetary mantle, *Nature*, *402*, 756–760.

Davaille, A., et al. (2005), Convective patterns under the Indo-Atlantic «box», *Earth Planet. Sci. Lett.*, *239*, 233–252.

Davies, G. F. (1999), *Dynamic earth: plates, plumes, and mantle convection*, 458 pp., Cambridge Univ. Press, New York.

Davies, G. F., and M. Gurnis (1986), Interaction of mantle dregs with convection—Lateral heterogeneity at the core mantle boundary, *Geophys. Res. Lett.*, *13*, 1517–1520.

Dziewonski, A. M., and D. L. Anderson (1981), Preliminary reference earth model, *Phys. Earth Planet. Inter.*, *25*, 297–356.

Farnetani, C. G. (1997), Excess temperature of mantle plumes: The role of chemical stratification across D″, *Geophys. Res. Lett.*, *24*, 1583–1586.

Farnetani, C. G., and H. Samuel (2005), Beyond the thermal plume paradigm, *Geophys. Res. Lett.*, *32*, L07311, doi:10.1029/2005GL022360.

Forte, A. M., and J. X. Mitrovica (2001), Deep-mantle high-viscosity flow and thermochemical structure inferred from seismic and geodynamic data, *Nature*, *410*, 1049–1056.

Garnero, E. J. (2000), Heterogeneity of the lowermost mantle, *Annu. Rev. Earth Planet. Sci.*, *28*, 509–537.

Garnero, E. J., and D. V. Helmberger (1996), Seismic detection of a thin laterally varying boundary layer at the base of the mantle beneath the central-Pacific, *Geophys. Res. Lett.*, *23*, 977–980.

Glatzmaier, G. A. (1988), Numerical simulations of mantle convection—Time-dependent, 3-dimensional, compressible, spherical-shell, *Geophys. Astrophys. Fluid Dyn.*, *43*, 223.

Gonnermann, H. M., M. Manga, and A. M. Jellinek (2002), Dynamics and longevity of an initially stratified mantle, *Geophys. Res. Lett.*, *29*(10), 1399, doi:10.1029/2002GL014851.

Grand, S. P., R. D. van der Hilst, and S. Widiyantoro(1997), Global seismic tomography: A snapshot of convection in the Earth, *GSA Today*, *7*, 1–7.

Gurnis, M. (1986), The effects of chemical density differences on convective mixing in the Earth's mantle, *J. Geophys. Res.*, *91*, 1407–1419.

Gurnis, M., J. X. Mitrovica, J. Ritsema, and H. van Heijst (2000), Constraining mantle density structure using geological evidence of surface uplift rates: The case of the African Superplume, *Geochem. Geophys. Geosyst.*, *1*, doi:10.1029/1999GC000035.

Hager, B. H., and R. J. O'Connell (1981), A simple global-model of plate dynamics and mantle convection, *J. Geophys. Res.*, *86*, 4843–4867.

Hama, J., and K. Suito (2001), Thermoelastic models of minerals and the composition of the Earth's lower mantle, *Phys. Earth Planet. Inter.*, *125*, 147–166.

Hansen, U., and D. A. Yuen (1988), Numerical simulations of thermal-chemical instabilities at the core mantle boundary, *Nature*, *334*, 237–240.
Hauri, E. H. (1996), Major-element variability in the Hawaiian mantle plume, *Nature*, *382*, 415–419.
Helmberger, D., T. Lay, S. Ni, and M. Gurnis (2005), Deep mantle structure and the postperovskite phase transition, *Proc. Natl. Acad. Sci. U. S. A.*, *102*, 17,257–17,263.
Hirose, K., R. Sinmyo, N. Sata, and Y. Ohishi (2006), Determination of post-perovskite phase transition boundary in $MgSiO_3$ using Au and MgO internal pressure standards, *Geophys. Res. Lett.*, *33*, L01310, doi:10.1029/2005GL024468.
Hirschmann, M. M., T. Kogiso, M. B. Baker, and E. M. Stolper (2003), Alkalic magmas generated by partial melting of garnet pyroxenite, *Geology*, *31*, 481–484.
Hofmann, A. W. (1997), Geochemistry—Early evolution of continents, *Science*, *275*, 498–499.
Hofmann, A. W., and W. M. White (1982), Mantle plumes from ancient oceanic crust, *Earth Planet. Sci. Lett.*, *57*, 421–436.
Hughes, T. J. R. (2000), *The Finite Element Method: Linear Static and Dynamic Finite Element Analysis*, 682 pp., Dover, Mineola, N. Y.
Ishii, M., and J. Tromp (1999), Normal-mode and free-air gravity constraints on lateral variations in velocity and density of Earth's mantle, *Science*, *285*, 1231–1236.
Ishii, M., and J. Tromp (2004), Constraining large-scale mantle heterogeneity using mantle and inner-core sensitive normal modes, *Phys. Earth Planet. Inter.*, *146*, 113–124.
Ita, J., and S. D. King (1994), Sensitivity of convection with an endothermic phase-change to the form of governing equations, initial conditions, boundary conditions, and equation of state, *J. Geophys. Res.*, *99*, 15,919–15,938.
Jacobsen, S. B., and G. J. Wasserburg (1979), The mean age of mantle and crustal reservoirs, *J. Geophys. Res.*, *84*, 7411.
Jarvis, G. T., and D. P. McKenzie(1980), Convection in a compressible fluid with infinite Prandtl number, *J. Fluid Mech.*, *96*, 515–583.
Jellinek, A. M., and M. Manga (2002), The influence of a chemical boundary layer on the fixity, spacing and lifetime of mantle plumes, *Nature*, *418*, 760–763.
Karato, S., and B. B. Karki (2001), Origin of lateral variation of seismic wave velocities and density in the deep mantle, *J. Geophys. Res.*, *106*, 21,771–21,783.
Kellogg, L. H., B. H. Hager, and R. D. van der Hilst (1999), Compositional stratification in the deep mantle, *Science*, *283*, 1881–1884.
King, S. D., A. Raefsky, and B. H. Hager (1990), Conman-vectorizing a finite-element code for incompressible 2-dimensional convection in the Earth's mantle, *Phys. Earth Planet. Inter.*, *59*, 195–207.
Kuo, B. Y., E. J. Garnero, and T. Lay (2000), Tomographic inversion of S-SKS times for shear velocity heterogeneity in D″: Degree 12 and hybrid models, *J. Geophys. Res.*, *105*, 28,139–28,157.
Kuo, C., and B. Romanowicz (2002), On the resolution of density anomalies in the Earth's mantle using spectral fitting of normal-mode data, *Geophys. J. Int.*, *150*, 162–179.
Lay, T., and D. Helmberger (1983), A lower mantle S-wave triplication and the shear velocity structure of D″, *Geophys. J. R. Astron. Soc.*, *75*, 799–837.
Lay, T., Q. Williams, and E. J. Garnero (1998), The core-mantle boundary layer and deep Earth dynamics, *Nature*, *392*, 461–468.
Lee, K. K., P. D. Asimow, and O. Tschauner (2005), Phase assemblage and stability of pyroxenite at lower-mantle conditions, *Eos Trans. AGU, Jt. Assem. Suppl.*, *86*, Abstract V42A-02.
Leitch, A. M., D. A. Yuen, and G. Sewell (1991), Mantle convection with internal heating and pressure-dependent thermal expansivity, *Earth Planet. Sci. Lett.*, *102*, 213–232.
Machetel, P., and D. A. Yuen (1989), Penetrative convective flows induced by internal heating and mantle compressibility, *J. Geophys. Res.*, *94*, 10,609–10,626.
Mao, W. L., et al. (2004), Ferromagnesian postperovskite silicates in the D″ layer of the Earth, *Proc. Natl. Acad. Sci. U. S. A.*, *101*, 15,867–15,869.
Marton, F. C., and R. E. Cohen (2002), Constraints on lower mantle composition from molecular dynamics simulations o $MgSiO_3$ perovskite, *Phys. Earth Planet. Inter.*, *134*, 239–252.
Masters, G., G. Laske, H. Bolton, and A. M. Dziewonski (2000), The relative behavior of shear velocity, bulk sound speed, and compressional velocity in the mantle: implications for chemical and thermal structure, in *Earth's Deep Interior*, edited by S. Karato, et al., pp. 63–87, AGU, Washington, D. C.
McNamara, A. K., and S. J. Zhong (2004), Thermochemical structures within a spherical mantle: Superplumes or piles?, *J. Geophys. Res.*, *109*, B07402, doi:10.1029/2003JB002847.
McNamara, A. K., and S. Zhong (2005), Thermochemical structures beneath Africa and the Pacific Ocean, *Nature*, *437*, 1136–1139.
McNutt, M. K. (1998), Superswells, *Rev. Geophys.*, *36*, 211–244.
Megnin, C., and B. Romanowicz (2000), The three-dimensional shear velocity structure of the mantle from the inversion of body, surface and higher-mode waveforms, *Geophys. J. Int.*, *143*, 709–728.
Montague, N. L., and L. H. Kellogg (2000), Numerical models of a dense layer at the base of the mantle and implications for the geodynamics of D″, *J. Geophys. Res.*, *105*, 11,101–11,114.
Montelli, R., et al. (2004), Finite-frequency tomography reveals a variety of plumes in the mantle, *Science*, *303*, 338–343.
Murakami, M., et al. (2004), Post-perovskite phase transition in $MgSiO_3$, *Science*, *304*, 855–858.
Murakami, M., K. Hirose, N. Sata, and Y. Ohishi (2005), Post-perovskite phase transition and mineral chemistry in the pyrolitic lowermost mantle, *Geophys. Res. Lett.*, *32*, L03304, doi:10.1029/2004GL021956.
Nakagawa, T., and P. J. Tackley (2004), Effects of a perovskite-post perovskite phase change near core-mantle boundary in compressible mantle convection, *Geophys. Res. Lett.*, *31*, L16611, doi:10.1029/2004GL020648.
Nakagawa, T., and P. Tackley (2005), The interaction between the post-perovskite phase change and a thermo-chemical boundary layer near the core-mantle boundary, *Earth Planet. Sci. Lett.*, *238*, 204–216.
Namiki, A. (2003), Can the mantle entrain D″?, *J. Geophys. Res.*, *108*(B10), 2487, doi:10.1029/2002JB002315.
Ni, S., E. Tan, M. Gurnis, and D. Helmberger (2002), Sharp sides to the African superplume, *Science*, *296*, 1850–1852.
Ni, S. D., and D. V. Helmberger (2003a), Seismological constraints on the South African superplume; could be the oldest distinct structure on Earth, *Earth Planet. Sci. Lett.*, *206*, 119–131.
Ni, S. D., and D. V. Helmberger (2003b), Ridge-like lower mantle structure beneath South Africa, *J. Geophys. Res.*, *108*(B2), 2094, doi:10.1029/2001JB001545.
Ni, S. D., and D. V. Helmberger (2003c), Further constraints on the African superplume structure, *Phys. Earth Planet. Inter.*, *140*, 243–251.
Nyblade, A. A., and S. W. Robinson (1994), The African Superswell, *Geophys. Res. Lett.*, *21*, 765–768.
Oganov, A. R., J. P. Brodholt, and G. D. Price (2001), The elastic constants of $MgSiO_3$ perovskite at pressures and temperatures of the Earth's mantle, *Nature*, *411*, 934–937.
Oganov, A. R., and S. Ono (2004), Theoretical and experimental evidence for a post-perovskite phase of $MgSiO_3$ in Earth's D″ layer, *Nature*, *430*, 445–448.
Olson, P., and C. Kincaid (1991), Experiments on the interaction of thermal-convection and compositional layering at the base of the mantle, *J. Geophys. Res.*, *96*, 4347–4354.
Ono, S., and A. R. Oganov (2005), In situ observations of phase transition between perovskite and $CaIrO_3$-type phase in $MgSiO_3$ and pyrolitic mantle composition, *Earth Planet. Sci. Lett.*, *236*, 914–932.
Quareni, F., W. Marzocchi, and F. Mulargia (1991), Anelastic convection in the mantle with variable properties, *Phys. Earth Planet. Inter.*, *68*, 117–131.
Ramage, A., and A. I. Wathen (1994), Iterative solution techniques for the Stokes and Navier-Stokes equations, *Int. J. Numer. Methods Fluids*, *19*, 67–83.
Resovsky, J. S., and J. Trampert (2003), Using probabilistic seismic tomography to test mantle velocity-density relationships, *Earth Planet. Sci. Lett.*, *215*, 121–134.
Richards, M. A., and D. C. Engebretson (1992), Large-scale mantle convection and the history of subduction, *Nature*, *355*, 437–440.
Ritsema, J., H. J. van Heijst, and J. H. Woodhouse (1999), Complex shear wave velocity structure imaged beneath Africa and Iceland, *Science*, *286*, 1925–1928.
Romanowicz, B. (2001), Can we resolve 3D density heterogeneity in the lower mantle?, *Geophys. Res. Lett.*, *28*, 1107–1110.
Rost, S., E. J. Garnero, Q. Williams, and M. Manga (2005), Seismological constraints on a possible plume root at the core-mantle boundary, *Nature*, *435*, 666–669.
Schmeling, H. (1989), Compressible convection with constant and variable viscosity—The effect on slab formation, geoid, and topography, *J. Geophys. Res.*, *94*, 12,463–12,481.
Schubert, G., G. Masters, P. Olson, and P. Tackley (2004), Superplumes or plume clusters?, *Phys. Earth Planet. Inter.*, *146*, 147–162.
Shampine, L. F., I. Gladwell, and S. Thompson (2003), *Solving ODEs with MATLAB*, 272 pp., Cambridge Univ. Press, New York.
Sidorin, I., M. Gurnis, and D. V. Helmberger (1999a), Dynamics of a phase change at the base of the mantle consistent with seismological observations, *J. Geophys. Res.*, *104*, 15,005–15,023.
Sidorin, I., M. Gurnis, and D. V. Helmberger (1999b), Evidence for a ubiquitous seismic discontinuity at the base of the mantle, *Science*, *286*, 1326–1331.

Solheim, L. P., and W. R. Peltier (1994), Avalanche effects in-phase transition modulated thermal-convection—A model of Earths mantle, *J. Geophys. Res.*, *99*, 6997–7018.

Steinbach, V., U. Hansen, and A. Ebel (1989), Compressible convection in the Earths mantle—A comparison of different approaches, *Geophys. Res. Lett.*, *16*, 633–636.

Sturhahn, W., J. M. Jackson, and J. F. Lin (2005), The spin state of iron in minerals of Earth's lower mantle, *Geophys. Res. Lett.*, *32*, L12307, doi:10.1029/2005GL022802.

Su, W. J., and A. M. Dziewonski (1997), Simultaneous inversion for 3-D variations in shear and bulk velocity in the mantle, *Phys. Earth Planet. Inter.*, *100*, 135–156.

Sun, D., E. Tan, D. Helmberger, and M. Gurnis (2007), Seismological support for the metastable superplume model, sharp features, and phase changes within the lower mantle, *Proc. Natl. Acad. Sci. U.S.A.*, doi:10.1073/pnas.0608160104.

Tackley, P. J. (1996), Effects of strongly variable viscosity on three-dimensional compressible convection in planetary mantles, *J. Geophys. Res.*, *101*, 3311–3332.

Tackley, P. J. (1998), Three-dimensional simulations of mantle convection with a thermo-chemical basal boundary layer: D″?, in *The Core-Mantle Boundary Region*, edited by M. Gurnis, et al., pp. 231–253, AGU, Washington, D. C.

Tackley, P. J. (2002), Strong heterogeneity caused by deep mantle layering, *Geochem. Geophys. Geosyst.*, *3*(4), 1024, doi:10.1029/2001GC000167.

Tan, E. (2006), I. Multi-scale Dynamics of Mantle Plumes, and II. Compressible Thermo-chemical Convection and the Stability of Mantle Superplumes, Ph.D. thesis, 180 pp., Calif. Inst. Tech., Pasadena, 2 May.

Tan, E., and M. Gurnis (2005), Metastable superplumes and mantle compressibility, *Geophys. Res. Lett.*, *32*, L20307, doi:10.1029/2005GL024190.

Tan, E., M. Gurnis, and L. J. Han (2002), Slabs in the lower mantle and their modulation of plume formation, *Geochem. Geophys. Geosyst.*, *3*(11), 1067, doi:10.1029/2001GC000238.

To, A., B. Romanowicz, Y. Capdeville, and N. Takeuchi (2005), 3D effects of sharp boundaries at the borders of the African and Pacific Superplumes: Observation and modeling, *Earth Planet. Sci. Lett.*, *233*, 137–153.

Trampert, J., F. Deschamps, J. Resovsky, and D. Yuen (2004), Probabilistic tomography maps chemical heterogeneities throughout the lower mantle, *Science*, *306*, 853–856.

Tsuchiya, J., T. Tsuchiya, and R. M. Wentzcovitch (2005), Vibrational and thermodynamic properties of $MgSiO_3$ postperovskite, *J. Geophys. Res.*, *110*, B02204, doi:10.1029/2004JB003409.

van der Hilst, R. D., S. Widiyantoro, and E. R. Engdahl (1997), Evidence for deep mantle circulation from global tomography, *Nature*, *386*, 578–584.

van Keken, P. E., et al. (1997), A comparison of methods for the modeling of thermochemical convection, *J. Geophys. Res.*, *102*, 22,477–22,495.

Wen, L. (2001), Seismic evidence for a rapidly varying compositional anomaly at the base of the Earth's mantle beneath the Indian Ocean, *Earth Planet. Sci. Lett.*, *194*, 83–95.

Wen, L., and D. V. Helmberger (1998), Ultra-low velocity zones near the core-mantle boundary from broadband PKP precursors, *Science*, *279*, 1701–1703.

Williams, Q., and E. J. Garnero (1996), Seismic evidence for partial melt at the base of Earth's mantle, *Science*, *273*, 1528–1530.

Xie, S., and P. J. Tackley (2004), Evolution of helium and argon isotopes in a convecting mantle, *Phys. Earth Planet. Inter.*, *146*, 417–439.

Zhang, S. X., and D. A. Yuen (1996), Various influences on plumes and dynamics in time-dependent, compressible mantle convection in 3-D spherical shell, *Phys. Earth Planet. Inter.*, *94*, 241–267.

M. Gurnis, Seismological Laboratory, California Institute of Technology, Pasadena, CA 91125, USA.

E. Tan, Computational Infrastructure for Geodynamics, Pasadena, CA 91107, USA. (tan2@gps.caltech.edu)